LBNL-51468

Inflow and Outflow Signatures in Flowing Wellbore Electrical-Conductivity Logs

Christine Doughty and Chin-Fu Tsang
Earth Sciences Division
E.O. Lawrence Berkeley National Laboratory
University of California

September 2002

Abstract

Flowing wellbore electrical-conductivity logging provides a means to determine hydrologic properties of fractures, fracture zones, or other permeable layers intersecting a borehole in saturated rock. The method involves analyzing the time-evolution of fluid electrical-conductivity logs obtained while the well is being pumped and yields information on the location, hydraulic transmissivity, and salinity of permeable layers, as well as their initial (or ambient) pressure head. Earlier analysis methods were restricted to the case in which flows from the permeable layers or fractures were directed into the borehole. More recently, a numerical model for simulating flowing-conductivity logging was adapted to permit treatment of both inflow and outflow, including analysis of natural regional flow in the permeable layer. However, determining the fracture properties with the numerical model by optimizing the match to the conductivity logs is a laborious trial-and-error procedure. In this paper, we identify the signatures of various inflow and outflow features in the conductivity logs to expedite this procedure and to provide physical insight for the analysis of these logs. Generally, inflow points are found to produce a distinctive signature on the conductivity logs themselves, enabling the determination of location, inflow rate, and ion concentration in a straightforward manner. Identifying outflow locations and flow rates, on the other hand, can be done with a more complicated integral method. Running a set of several conductivity logs with different pumping rates (e.g., half and double the original pumping rate) provides further information on the nature of the feed points. In addition to enabling the estimation of flow parameters from conductivity logs, an understanding of the conductivity log signatures can aid in the design of follow-up logging activities.

1. Introduction

In the study of flow and transport through fractured rocks, knowledge of the locations of fractures and their hydraulic properties is essential. Often such knowledge is obtained using deep boreholes penetrating the fractured rock. Among the various downhole methods of determining fracture properties that have been developed over the past few decades, flowing wellbore electrical conductivity-logging has proved to be quite useful (Tsang et al., 1990). In this method, the wellbore water is first replaced by de-ionized water or, alternatively, water of a constant salinity distinctly different from that of the formation water. This is done by passing the de-ionized water down a tube to the bottom of the borehole at a given rate, while simultaneously pumping from the top of the well at the same rate, for a short time period. Next, the well is shut in or pumped from the top at a constant low flow rate (e.g., tens of liters per minute), while an electric conductivity probe is lowered into the borehole to scan the fluid electric conductivity (FEC) as a function of depth. This produces what is known as an FEC log. With constant pumping conditions, a series of five or six FEC logs are typically obtained over a one- or two-day period. At depth locations where water enters the borehole (the feed points), the FEC logs display peaks. These peaks grow with time and are skewed in the direction of water flow. By analyzing these logs, it is possible to obtain the flow rate and salinity of groundwater inflow from the individual fractures. The method is more accurate than spinner flow meters and much more efficient than packer tests (Tsang et al., 1990).

Although we often refer to feed points as representing flow through hydraulically conductive fractures, they can just as easily represent flow through any permeable zone that intersects the wellbore section being logged. In heterogeneous porous media such as alluvial systems composed of interspersed sand and clay lenses, flow can be just as localized as in

fractured rock, and the need for identifying permeable strata just as great. The method developed in this paper is equally applicable to such heterogeneous media.

Figure 1.1 shows a typical series of FEC logs obtained from a 230 m well (Colog, Inc., personal communication, 1999). Key features apparent in the logs include (a) an isolated peak at a depth of 164 m with an unusually sharp upper limb; (b) several interfering peaks in the depth range of 174–187 m; and (c) an overall downward propagation of peaks below a depth of 164 m. The goal of the present study is to investigate the typical signatures in FEC logs produced by different combinations of feed points and flow conditions. Further, integral measures will be derived from the FEC logs, to facilitate analysis of logs such as these.

Existing tools for analyzing flowing wellbore FEC logs include analytical solutions, numerical modeling, and integral approaches. Simple analytical solutions based on mass balances can be used to infer feed-point properties at early times before peaks interfere with each other (Tsang et al., 1990); under steady-state conditions when peaks fully interfere (Tsang et al., 1990); and for the special case of horizontal flow (Drost et al., 1968). These solutions provide useful information when used as part of a more sophisticated analysis (as described in Section 2), but by themselves are too simplistic for most real-world problems.

The numerical model BORE (Hale and Tsang, 1988; Tsang et al., 1990) and the recently enhanced version BORE II (Doughty and Tsang, 2000) calculate the time evolution of ion concentration (salinity) through the wellbore, given a set of feed-point locations, strengths, and concentrations (i.e., the forward problem). BORE II broadens the range of applicability of the analytical solutions described above by considering multiple inflow and outflow feed points, isolated and overlapping FEC peaks, early-time and late-time behavior, time-varying feed-point strengths and concentrations, and the interplay of advection and diffusion in the wellbore. The

Appendix presents the governing equations used by BORE II. Using BORE II to match observed FEC profiles (the inverse problem) requires the trial-and-error adjustment of feed-point parameters. This can be a difficult and time-consuming process, especially for noisy data. Several integral approaches have been developed (Tsang and Hale, 1989; Loew et al., 1990) that can provide good initial guesses to BORE, greatly enhancing its ease of use. However, these methods are limited to wellbore sections containing inflow points only. Thus, for example, they are not applicable to cases of horizontal flow across the well diameter or internal wellbore flow. The motivation for the current investigation of feed-point signatures is threefold. First, we want to develop a method for making zero-order parameter estimates for the general case in which inflow and outflow points exist. These can be used as good initial guesses for BORE II, in order to expedite the analysis of wellbore FEC logs. Second, we want to obtain physical insight into the nature of the feed points from particular features or signatures in the FEC logs. Third, we want to determine the optimal scheme for collecting new data by investigating how the choice of pumping rate can enhance feed-point signatures. Differences in feed-point strengths among various permeable layers or fractures reflect differences in local hydraulic transmissivity values or pressures or both, and by varying the pumping rate we can discriminate between these cases. In Section 2, we examine the typical signatures observed in a wellbore FEC log, and determine what they tell us about the feed-point parameters. For inflow points we look at the FEC profile itself, while for outflow points we introduce an integral analysis. Section 3 investigates the effect of pumping rate on these signatures, both to decide on the optimal pumping rate for log interpretation and to investigate the nature of feed points. Section 4 illustrates the application of the techniques by analyzing FEC logs obtained from two field sites. Section 5 summarizes the material and presents some concluding remarks.

2. Signatures of Inflow and Outflow Points

The signatures of individual inflow feed points and various combinations of inflow and outflow feed points contain both qualitative and quantitative information about the feed-point parameters, which can be used to improve the initial parameter values for a BORE II simulation. In these discussions, we refer to concentration profile $C(x)$, which is the ion concentration of borehole fluid as a function of depth x. The conversion of an FEC log, $\sigma(x)$, to a concentration profile, $C(x)$, is described in the Appendix. Boreholes that contain only inflow feed points produce the most straightforward $C(x)$ signatures. The signatures of outflow feed points are generally difficult to see in the $C(x)$ profiles, and therefore a more elaborate mass-integral technique has been developed for cases in which both inflow and outflow points exist.

2.1 Concentration Profiles

The four quantities that need to be determined for each feed point are location x_i, inflow or outflow rate q_i (positive for inflow and negative for outflow), and, for inflow points, concentration C_i and the time t_{0i} at which feed-point concentration first differs from the initial wellbore concentration C_0. Often $t_{0i} = 0$, but a non-zero value can occur if de-ionized water migrates into the fracture during the initialization phase of replacing borehole water prior to wellbore logging, or if wellbore logging takes place during a tracer test in which a saline tracer arrives from a nearby well or source.

2.1.1 Inflow Points

Figure 2.1 shows a series of idealized concentration profiles simulated with the numerical model BORE II, using feed points with constant $q_i > 0$, constant $C_i > C_0$, and $t_{0i} = 0$. Factors such as

upflow from the bottom of the wellbore section, time-dependent feed points, inflow points with $C_i = C_0$, and outflow points are discussed separately in later subsections.

The first step is to locate the feed points. Inflow points can usually be located fairly accurately from early-time concentration profiles, when each inflow point produces a small, isolated concentration peak. In the calculated example shown in Figure 2.1, inflow points are apparent at depths of 60, 90, and 120 m (see also Figures 4.1 and 4.5 for field examples).

For inflow points, the estimation of q_i and C_i is best done concurrently, because these quantities have a coupled effect on $C(x)$. For early-time data, before inflow peaks begin to interfere with each other, mass conservation requires that at time t, the ion mass represented by the ith concentration peak, $M_i(t)$, be given by

$$M_i(t) = q_i C_i t, \tag{2.1}$$

where we assume for simplicity that $C_0 = 0$. Therefore, the area under the ith $C(x)$ peak can be expressed as

$$A_i = \int C(x)dx = \frac{M_i(t)}{\pi r^2} = \frac{q_i C_i t}{\pi r^2}, \tag{2.2}$$

where r is the wellbore radius. Calculating A_i by numerically integrating the $C(x)$ profile in the vicinity of the ith feed point, at a series of times, can be done to estimate the product $q_i C_i$ and to verify that it is constant in time. Very early profiles, which show small peaks, generally provide less accurate integrals than do larger peaks. As a rule, the largest noninterfering peaks should be used to estimate the $q_i C_i$ product. Table 2.1 summarizes the $q_i C_i$ products obtained for the peaks shown in Figure 2.1.

At intermediate times, because the well bottom is closed to flow, peaks become skewed toward the top of the well. In principle, such skewness can be used to separate q_i and C_i. This

can be done by fitting to numerical results from BORE II in which q_i and C_i are varied, while keeping their product constant.

At late times, the concentration profile reaches a steady-state condition consisting of a series of steps with concentration $C_{\max i}$, each associated with an inflow point. For the lowest inflow point (x_1, q_1, C_1) in a wellbore section closed at the bottom, the steady-state concentration $C_{\max 1}$ is equal to C_1. Mixing rules dictate that the second-lowest inflow point (x_2, q_2, C_2, with $x_2 < x_1$) has $C_{\max 2}$ given by

$$C_{\max 2} = \frac{q_1 C_1 + q_2 C_2}{q_1 + q_2}. \tag{2.3}$$

Generally, for the ith inflow point,

$$C_{\max i} = \frac{\sum q_j C_j}{\sum q_j}, \tag{2.4}$$

where the sums are taken over all feed points with $x_j \geq x_i$. This expression can be solved for q_i,

$$q_i = \frac{\sum q_j C_j}{C_{\max i}} - \sum q_k , \tag{2.5}$$

where the j sum is taken over all feed points with $x_j \geq x_i$ and the k sum is taken over all feed points with $x_k > x_i$. Finally, we determine C_i from the $q_i C_i$ product and q_i:

$$C_i = \frac{(q_i C_i)}{q_i}. \tag{2.6}$$

Hence, observing $C_{\max 1}$ gives us C_1, and using the value of the $q_1 C_1$ product from the early-time data determines q_1. Then, knowing $q_1 C_1$, $q_2 C_2$, q_1, and $C_{\max 2}$ enables us to determine q_2 and C_2. We continue this way up the wellbore section until all feed-point properties are

determined. Table 2.1 summarizes the C_{maxi}, q_i, and C_i values for the feed points shown in Figure 2.1. Note that any errors introduced at lower feed points influence the results for shallower feed points, so the accuracy of the properties may decrease as we move up the wellbore. A consistency check is provided by comparing the sum of all the feed-point inflow rates Σq_i to the pumping rate from the top of the wellbore section Q, which is a known quantity prescribed as part of the logging procedure. If these two quantities do not agree, there are two possible remedies. If all the feed points show equally good plateaus, then all the inflow rates can be scaled by $Q/\Sigma q_i$. On the other hand, a common situation is for logging to end before the uppermost (Nth) peak reaches steady state, in which case Q can simply be used in place of Σq_i in Equation (2.4) to determine C_{maxN}. Note particularly that to use Q as a constraint, care must be taken that it does not include unknown contributions from inflow into the wellbore above the logged section being analyzed. This can easily happen in actual field conditions.

If we have reason to believe that the C_i for all inflow points are the same (say $C_i = C$), then Equation (2.4) gives $C_{maxi} = C$, implying that steady-state concentration profiles do not provide any new information. In fact, for this special case, it is possible to determine all the q_i values and C from early-time profiles only. First, the early-time profiles are used to determine the q_iC product for each feed point as usual. Then, the equation $Q = \Sigma q_i$ is multiplied by C on both sides,

$$CQ = C\sum q_i = \sum q_i C \tag{2.7}$$

and solved for C

$$C = \frac{\sum q_i C}{Q}. \tag{2.8}$$

Finally, Equation (2.6) is used to determine each value of q_i from the q_iC product and C.

Another potential simplification occurs if the feed points are far enough apart for $C(x)$ plateaus to develop before the peaks begin to interfere with one another, as shown for the two shallower peaks in Figure 2.1a at 90 minutes and in Figure 2.1b at 0.1 day. The isolated plateau concentration is denoted $C_{\mathrm{mid}i}$, and is given by an equation similar to Equation (2.4) for $C_{\mathrm{max}i}$

$$C_{midi} = \frac{q_i C_i}{\sum q_j} \tag{2.9}$$

where the denominator sum runs over all $x_j \geq x_i$. Expressions for q_i and C_i analogous to Equations (2.5) and (2.6) follow directly, enabling determination of q_i and C_i for the ith peak, given $C_{\mathrm{mid}i}$ and the q_iC_i products for the ith and all deeper peaks. Note that for the lowest peak, $C_{\mathrm{mid}1} = C_{\mathrm{max}1} = C_1$.

2.1.2 Upflow from Below

Upflow from below can occur when the bottom of the wellbore interval being investigated is not the actual bottom of the well and is not sealed with a packer. If upflow from below has a distinctive salinity, it can be treated as any other inflow point, but if it has salinity C_0, it will not produce a peak of its own and its presence must be inferred from its influence on the other peaks. Figure 2.2 shows the BORE II concentration profiles obtained using the same feed-point parameters as for Figure 2.1, but with the addition of upflow from below at a rate q_w and a concentration C_0. Comparing Figures 2.2 and Figure 2.1 shows that the peaks are all more strongly skewed upward when $q_w > 0$. The most evident change occurs at the lower limb of the lowest peak, which shows a diffusive profile when $q_w = 0$ (Figure 2.1) and a combination of advection and diffusion when $q_w > 0$ (Figure 2.2). Integration under the early-time $C(x)$ peaks

provides q_iC_i estimates as before, despite the asymmetric shape of peaks, but, since the peaks interfere sooner, care must be taken in the choice of the profiles to integrate.

The steady-state mixing rule for the ith feed point becomes

$$C_{\max i} = \frac{\sum q_j C_j}{q_w + \sum q_j}, \tag{2.10}$$

where as before, the sums are taken over all feed points with $x_j \geq x_i$. If the peaks develop plateaus before they begin to interfere with one another, Equation (2.9) for $C_{\mathrm{mid}i}$ can be modified by adding q_w to the denominator. In either case, we have a system of equations with one more unknown than number of equations (if Q is not used); therefore, we cannot determine all the feed-point parameters individually. However, we can determine the sum $q_1 + q_w$ and individual values of q_i and C_i for feed points above the lowest one. We still have $C_{\mathrm{mid}1} = C_{\max 1}$, but with a non-zero q_w, $C_{\max 1} \neq C_1$. Comparing the different C_i values might provide insight into the likely range for C_1, enabling an estimate of q_1 to be made. Furthermore, if we have an independent estimate of C_1, q_1, or q_w, then we can determine the remainder of the feed-point parameters. As before, wellbore pumping rate Q may be used to constrain feed-point properties by requiring $Q = q_w + \Sigma q_i$, where the sum runs over all feed points. Again, in doing this care must be taken that Q does not include unknown possible inflows into the wellbore above the logged section.

2.1.3 Time-Dependent Feed Points

Time-dependent values of q_i and C_i most commonly arise when pumping rates are altered or tracers are introduced in nearby wells. However, they can also represent actual physical or chemical variations in the rock near the borehole. Figure 2.3 shows the BORE II concentration profiles for a single inflow point in which feed-point concentration is either constant at C_1 (Figure 2.3a), increases linearly from 0 to C_1 (Figure 2.3b), or decreases linearly from C_1 to 0

(Figures 2.3c and d). A decreasing feed-point concentration provides a distinctive concentration profile signature, particularly when combined with upflow. In contrast, the profiles for increasing feed-point concentration or increasing feed-point inflow rate (not shown) may be difficult to distinguish from those for a constant feed point. For early times, before the profiles for adjacent inflow points begin to interfere with each other, we can generalize Equation (2.1) for $M_i(t)$ to obtain

$$M_i(t) = \int_0^t q_i(t')C_i(t')dt' . \qquad (2.11)$$

Hence, the slope of the $M_i(t)$ versus t curve gives $q_i(t)C_i(t)$. This approach does not distinguish between time dependencies in q_i or C_i separately, but the skewness of concentration peaks, which depends only on q_i, may provide insight into q_i and C_i time variations. If either q_i or C_i is known to be constant, then Equation (2.11) can be used to calculate the time dependence of the other quantity.

A common feed-point time dependence, which arises if de-ionized water migrates into the fracture during the replacement of borehole water prior to wellbore logging, is for both q_i and C_i to be constant after a time t_{0i}, but to have $C_i = C_0$ before t_{0i}. In this case, it is generally possible to estimate t_{0i} along with q_iC_i by integrating over a series of profiles and fitting the resulting $M_i(t)$ values to the linear relation

$$M_i(t) = q_iC_i(t - t_{0i}). \qquad (2.12)$$

2.1.4 Inflow Points with $C_i = C_0$

It may happen that the initial wellbore ion concentration is similar to some of the feed point concentrations, i.e., for some feed points, $C_i = C_0$. An inflow point with $C_i = C_0$ does not

produce a concentration peak of its own, but its effect on neighboring peaks may be visible. Figure 2.4 shows the BORE II concentration profiles for two inflow points, one of which has $C_i = C_0$. In each of the four examples in Figure 2.4, the inflow rate of the $C_i = C_0$ inflow point is twice that of the adjacent inflow point. If the $C_i = C_0$ inflow point is above (downstream of) the other inflow point, there is a subtle signature in the form of a break in slope of the concentration profiles when the diluting effect of the $C_i = C_0$ inflow is first felt (Figure 2.4a). This break in slope is accentuated if an upflow from below is present (Figure 2.4b). At late times, the $C_i = C_0$ inflow point causes a distinctive plateau (Figure 2.4c). If the $C_i = C_0$ inflow is below (i.e., up-stream of) the other inflow point, the break in slope is difficult to see (Figure 2.4d). The concentration profile is skewed upward as when an upflow is present; this identifies the existence of a $C_i = C_0$ inflow, but not its location.

2.1.5 Outflow Points

Outflow may occur when the far-field heads in certain fractures or permeable zones penetrated by a wellbore are different. When the well is shut in or is pumping at a very low rate, water flows into the wellbore from the higher head zone, is transmitted through the wellbore, and flows out into a lower-head zone. Figure 2.5 shows the BORE II concentration profiles for an outflow point located adjacent to an inflow point. In each example, the outflow strength is twice the inflow strength. The outflow points cause subtle changes in the shape of the peaks, but these changes do not identify the outflow location well. The addition of an upflow changes the peak shape, but does not help pin down the outflow location. An integral method that can estimate the outflow location is presented in the next section.

Figure 2.6 shows the BORE II concentration profiles for inflow and outflow points located farther apart, with profiles collected frequently enough to monitor the movement of the

concentration front up the wellbore. In this case, $q_1 \equiv q_{in}$, $q_2 \equiv q_{out}$, and q_w all have the same magnitude and $q_{out} = -q_{in}$, so the speed of the front is halved as it passes the outflow point. By examining the spacing between concentration profiles obtained at known time intervals, the location of the outflow point can be inferred.

2.1.6 Horizontal Flow

Measurement of horizontal flow across the wellbore is important because it can be used to estimate the natural regional flow in the hydrologic layer (Drost et al., 1968). In our case, horizontal flow can be represented with a pair of inflow and outflow feed points located at the same depth, with $q_1 \equiv q_{in} = Q_0$ and $q_2 \equiv q_{out} = -Q_0$, where Q_0 is the volumetric flow rate across the wellbore. Q_0 can be related to the regional Darcy velocity v_d in the layer intercepted by the wellbore using $Q_0 = v_d 2rb\alpha_h$, where r is the wellbore radius, b is the thickness of the hydrologic layer, and α_h is a dimensionless convergence factor ranging from 1 to 4, which depends on well completion (Drost et al., 1968). Figure 2.7 compares the BORE II concentration profiles for several horizontal-flow cases with the corresponding case in which only an inflow feed point with strength q_{in} is present. Unlike previous plots that show successive concentration profiles at equally spaced time intervals, here the time interval doubles between each successive profile, to enable both early- and late-time behavior to be illustrated in a single plot. At early times, the concentration profiles for inflow and horizontal flow are similar, both showing symmetric profiles. At later times, the horizontal-flow profiles remain symmetric, whereas the inflow profiles become skewed up the wellbore. Peak concentration increases faster with inflow only, but in the absence of longitudinal diffusion, the steady-state concentration C_{max} would be $C_1 \equiv C_{in}$ for both cases.

Figures 2.7a and 2.7b depict a typical situation in which diffusion along the wellbore is moderately strong compared to horizontal-flow or inflow strength (practically, the movement of the conductivity logging tool up and down the wellbore greatly enhances the longitudinal diffusion coefficient D_0 over the value for still water). Figures 2.7c and 2.7d illustrate how the concentration profiles sharpen when D_0 is very small. Figures 2.7e and 2.7f show the profiles for thick layers of inflow and horizontal flow, modeled by placing multiple inflow points or inflow/outflow pairs over a range of x values. The value of D_0 is moderate, as in Figures 2.7a and 2.7b, but at the center of the flow layer it has little impact, allowing the concentration profiles to reach $C_{max} = C_{in}$. The black dots on the horizontal-flow profiles in Figure 2.7f show the concentration given by an analytical solution (Drost et al., 1968) that considers horizontal flow only (i.e., longitudinal diffusion is negligible or the hydrologic flow layer is very thick):

$$C(t) = C_{in} - [C_{in} - C_0] \exp\left(\frac{-2tv_d \alpha_h}{\pi r} \right). \qquad (2.13)$$

The BORE II simulation of a thick horizontal-flow layer matches the analytical solution well. Figure 2.8 shows $C(t)/C_{in}$ at the center of the flow layer as a function of time for the cases shown in Figures 2.7b, d, and f, as well as for a thick layer with very small D_0 and the Drost et al. (1968) solution itself. Both thick-layer cases follow the analytical solution closely, regardless of the value of D_0 applied, and the thin-layer case with very small D_0 shows similar behavior. However, for a thin layer (such as a narrow conducting zone or a single fracture) with a realistic value of D_0, the peak concentration grows much more slowly. Diffusion plays a significant role, decreasing the concentration at the feed-point concentration by effectively mixing formation water with wellbore water. In this case, matching with BORE II will yield a more accurate estimate of horizontal flow than Drost's solution.

2.2 Mass Integrals

The examples of concentration profiles shown in the previous section indicate that in general, outflow points do not produce a strong signature that enables them to be easily located. Here, we describe an integral procedure that enables outflow points to be located by examining changes in ion mass in the wellbore section.

Consider a wellbore section with one or more outflow points above one or more inflow points. Let us assume feed-point strength and concentration do not vary in time. The procedure is as follows. We integrate each $C(x)$ profile over the entire wellbore section of interest to obtain the area $A(t)$ under the $C(x)$ profile at time t (including all peaks, whether or not they interfere). Then, we multiply $A(t)$ by the mean wellbore cross-sectional area to determine ion mass in place at time t, which we denote as the mass integral $M(t)$, and plot $M(t)$ versus t. Note that before the concentration front reaches any outflow points, $M(t)$ is linear, with slope

$$S_{\text{early}} = \sum_{in} q_i C_i \ . \tag{2.14}$$

When the concentration front reaches an outflow point, the slope of $M(t)$ decreases, since ion mass leaves the wellbore at that point. When the concentration front passes the uppermost outflow point, $M(t)$ becomes linear again, with slope

$$S_{\text{late}} = \sum_{in} q_i C_i - \sum_{out} q_i C_{\max i} = S_{\text{early}} - C_{\max} \sum_{out} q_i \ , \tag{2.15}$$

where $C_{\max}$ is the maximum concentration at the uppermost outflow point. To determine the aggregate outflow rate, we rearrange Equation (2.15) to yield

$$\sum_{out} q_i = \frac{S_{early} - S_{late}}{C_{\max}} . \tag{2.16}$$

Now, let us examine the $C(x)$ profiles and locate the times when (a) $M(t)$ becomes nonlinear and (b) $M(t)$ becomes linear again. The leading edge of the concentration front at (a) identifies the

deepest outflow point, x_{max}. The trailing edge of the concentration front at (b) identifies the shallowest outflow point, x_{min}. Here, we define the leading edge as the x location at which $C(x) = 0.1C_{max}$ and the trailing edge as the x location at which $C(x) = 0.9C_{max}$.

An example of the mass-integral procedure for early-time concentration profiles is shown in Figure 2.9. We consider a single inflow point located below a single outflow point in a wellbore section with upflow from below. The BORE II concentration profiles (Figure 2.9a) contain a minor break in slope at the outflow point, which would probably be impossible to identify in real data. In contrast, the mass-integral plot (Figure 2.9b) shows a clear divergence from linearity between $t = 0.4$ and $t = 0.6$ days. Returning to the $C(x)$ profiles, we find that the leading edges of the $t = 0.4$-day and $t = 0.6$-day profiles lie at $x = 84$ and $x = 82.5$ m, respectively. Since the $t = 0.4$-day integral fits the linear $M(t)$ trend but the $t = 0.6$-day integral does not, we infer that the outflow point occurs at $82.5 \leq x \leq 84$ m. The actual location of the outflow point is 84.5 m. Hence the $M(t)$ method, while not perfect, does provide useful information for outflow-point location.

Another example, this time considering long-time concentration profiles, is shown in Figure 2.10. We consider two inflow points located below two outflow points in a wellbore section with upflow from below. The BORE II concentration profiles (Figure 2.10a) show interference between two inflow peaks, which makes it difficult to simply locate the outflow points by inspection. The mass-integral plot (Figure 2.10b) shows early-time and late-time linear sections, with a slight departure from linearity for $t = 0.3$ days and a return to linearity by $t = 0.7$ days. The leading edge of the $t = 0.3$-day profile lies at $x = 65$ m, suggesting that the deepest outflow point is just below this depth. The trailing edge of the $t = 0.07$-day profile lies at $x = 50$ m, suggesting that the shallowest outflow point is just below this depth. These predictions are

reasonably close to the actual locations of the outflow points, 70.5 and 50.5 m. Using Equation (2.16) with the values of S_{early}, S_{late}, and C_{max} shown in Figure 2.10 yields an aggregate outflow rate of 1.48 L/min, which agrees closely with the actual value, 1.5 L/min.

Note that in theory, if two outflow points are separated by a large enough distance, a linear portion in the $M(t)$ plot will develop when the concentration fronts are between the two points, potentially enabling the locations and strengths of the individual points to be determined. However, if the two points are separated by a distance comparable to or less than the width of the concentration fronts, as in Figure 2.10, the $M(t)$ method will not be able to resolve them.

3. Effect of Pumping Rate

The previous section showed that the flow rate in the wellbore interval of interest has a strong effect on the signature of the peaks. Since we have control of the flow rate through the selection of the well pumping rate Q for a given conductivity log, the choice of Q or the use of two logging runs with different Q values may be used to improve the accuracy of parameter determination. To study this effect systematically, we need to understand how feed-point strength changes when Q is modified. This dependence is derived below for several practical cases of interest, followed by examples illustrating how Q affects $C(x)$ profiles and $M(t)$ integrals. We then discuss how modifying Q may be used to investigate the nature of the feed points.

3.1 How Feed-Point Strength Depends on Q

We consider a wellbore interval containing N feed points. The strength of the ith feed point is q_i and $\Sigma q_i = Q$. By convention, inflow points have positive q_i and outflow points have negative q_i. Upflow from below can be absent (i.e., the lower end of the studied interval is the well bottom or

sealed by a packer) or represented by one of the N feed points (upflow is positive and downflow negative). For each feed point, q_i and concentration C_i are assumed to be constant in time. The strength of a feed point is related to its hydraulic transmissivity T_i^*, the "far-field" pressure P_i a distance r_i away from the wellbore, and the pressure P_{wb} at the wellbore radius r through Darcy's law. Assuming steady radial flow into the wellbore,

$$q_i = \frac{2\pi T_i^* (P_i - P_{wb})}{\ln(r_i / r)} = T_i (P_i - P_{wb}) , \tag{3.1}$$

where T_i represents an effective hydraulic transmissivity, into which the constant factors involving radial distance have been lumped. T_i is introduced to simplify notation. For the special case of horizontal flow with net $q_i = 0$, the log dependence on r is replaced by a linear dependence, but the right-side form (containing only T_i and pressure) is unchanged. We assume that the hydraulic transmissivity within the wellbore itself is much greater than that of any inflow zone, so that P_{wb} is constant over the wellbore interval of interest. Since $\Sigma q_i = Q$, we can write

$$Q = \sum T_i (P_i - P_{wb}) . \tag{3.2}$$

If we now alter the pumping rate from Q to Q', T_i and P_i remain unchanged but P_{wb} becomes P_{wb}', and

$$q_i' = T_i (P_i - P_{wb}') \tag{3.3}$$

$$Q' = \sum T_i (P_i - P_{wb}') . \tag{3.4}$$

We solve Equation (3.4) for P_{wb}' and substitute into Equation (3.3), yielding an expression for q_i' in terms of Q':

$$q_i' = T_i P_i - \frac{T_i (-Q' + \sum T_i P_i)}{\sum T_i} . \tag{3.5}$$

Adding and subtracting the term $T_i P_{wb}$ to Equation (3.5) and then substituting from Equations (3.1) and (3.2), we obtain

$$q_i' = q_i + \frac{T_i(Q'-Q)}{\sum T_i}. \tag{3.6}$$

Defining $\Delta q_i = q_i' - q_i$, $\Delta Q = Q' - Q$, and $T_{tot} = \Sigma T_i$ yields the more compact form

$$\Delta q_i = \frac{T_i \Delta Q}{T_{tot}}, \tag{3.7}$$

which is the fundamental relationship between the change in feed-point strength Δq_i and the change in pumping rate ΔQ. Note that Δq_i is directly proportional to T_i, and thus the feed points with larger hydraulic transmissivity show greater changes in strength when Q is modified. In particular, if the jth feed point has a much larger hydraulic transmissivity than all the others ($T_j \approx T_{tot}$), then $\Delta q_j \approx \Delta Q$ and all the other feed-point strengths will not change much. This situation might arise if the well intercepts an extensive inflow zone that has not been excluded from the logging section by packers.

There are several special cases of Equation (3.7) that are of interest. If all the T_i's are the same, then $T_i = T_{tot}/N$, and Equation (3.7) simplifies to

$$\Delta q_i = \frac{\Delta Q}{N}, \tag{3.8}$$

where N is the number of feed points. In this case, when Q is modified, all feed-point strengths change by the same amount.

A particular case of the equal T_i condition is horizontal flow across the wellbore, where $Q = 0$, N = 2, $q_{in} = Q_0$, and $q_{out} = -Q_0$. Thus, if pumping is added to a horizontal-flow case ($\Delta Q > 0$), inflow points become stronger ($q_{in}' = Q_0 + \Delta Q/2$) and outflow points become weaker ($q_{out}' = -Q_0 + \Delta Q/2$). When $\Delta Q/2 > Q_0$, q_{out}' changes sign and the outflow points become inflow points. For

a thick layer, N can be any even number. In that case, initially $Q = 0$, $q_{in} = 2Q_0/N$, $q_{out} = -2Q_0/N$, and then when pumping at rate ΔQ is imposed, $q_{in}' = (2Q_0 + \Delta Q)/N$ and $q_{out}' = (-2Q_0 + \Delta Q)/N$. On the other hand, if the P_i's are all the same, then we solve Equation (3.1) for T_i and substitute into Equation (3.7)

$$\Delta q_i = \frac{\Delta Q q_i}{T_{tot}(P_i - P_{wb})} = \frac{\Delta Q q_i}{Q}. \tag{3.9}$$

Note that when all P_i's are the same, feed points must be either all inflow points or all outflow points, and there can be no horizontal or internal flow. In this case, when Q is modified, the relative change of each feed point $\Delta q_i/q_i$ is the same and is equal to the relative change of Q,

$$\frac{\Delta q_i}{q_i} = \frac{\Delta Q}{Q}. \tag{3.10}$$

Thus, feed points can only change sign if Q changes sign (i.e., pumping becomes injection), and then they all will change sign, again precluding horizontal or internal flow.

Finally, if all the T_i's are the same and all the P_i's are the same, then according to Equation (3.1), all the q_i's must be the same. Thus, $q_i = Q/N$, and Equations (3.8) and (3.9) become equivalent.

3.2 Examples of How Modifying Q Affects C(x) and M(t) Signatures

Running FEC logs with two or more values of Q (for example, halving and doubling the original pumping rate) should provide a means to better characterize the feed points for cases with inflow points only, cases with both inflow and outflow points, and for the special case of horizontal flow.

Figure 3.1 shows the effect of increasing Q on a single inflow point with a constant strength and concentration. With a low Q (Figure 3.1a), only the $q_{in}C_{in}$ product can be determined. With a larger Q (Figure 3.1b), evidence of the C_{max} plateau develops at an earlier time, enabling

determination of C_{in} and q_{in} independently. Note that, in the absence of longitudinal diffusion, increasing or decreasing Q would be completely equivalent to logging for a longer or shorter period of time, respectively.

Figure 3.2 shows the effect of modifying Q when both inflow and outflow points are present and all T_i's are the same. For the original Q value (Figure 3.2a), the outflow point produces only a subtle change in slope in the $M(t)$ plot, making the mass-integral procedure difficult. If Q is halved (Figure 3.2b), the change in slope becomes larger and the analysis becomes straightforward. On the other hand, if Q is doubled (Figure 3.2c), the outflow point becomes an inflow point and is easily identified in the early-time $C(x)$ profiles as another peak. Finally, if Q is reduced to zero (Figure 3.2d), then the outflow point must capture all the flow in the wellbore, and again the $C(x)$ profiles would provide a strong signature of the outflow point.

Figure 3.3 shows the effect of increasing Q on a thin layer with horizontal flow, where initially (Figure 3.3a) $Q = 0$, $q_{in} = Q_0$ and $q_{out} = -Q_0$. The T_i's for the inflow and outflow points are the same, and hence, as Q is increased from zero, the magnitude of q_{in} increases and the magnitude of q_{out} decreases (Figures 3.3b and 3.3c). When $Q = 2Q_0$, outflow vanishes (Figure 3.3d), and when $Q > 2Q_0$, the outflow point becomes an inflow point.

Figure 3.4 shows the effect of increasing Q on the horizontal-flow case when an upflow from below q_w accompanies the increase in Q. We assume that when $Q = 0$, $q_w = 0$, $q_{in} = Q_0$, $q_{out} = -Q_0$, and the concentration profiles are as shown in Figure 3.3a. One possible approach is to consider q_w as arising from a single deep feed point with a T value equal to that of the inflow/outflow pair used to model horizontal flow (Figures 3.4a, c, and e). As Q is increased, $\Delta q = \Delta Q/3 = Q/3$ for each of the three feed points, so the inflow strength and upflow increase while the outflow strength decreases. The steady-state plateau concentration is given by

$$C_{\max} = \frac{q_{in}C_{in}}{q_{in} + q_w} = \frac{(Q_0 + Q/3)C_{in}}{Q_0 + 2Q/3}. \tag{3.11}$$

Another approach is to associate upflow with a very large T value, which is equivalent to considering upflow as arising from many individual feed points or an extensive inflow zone (Figures 3.4b, d, and f). In this case, the increase in Q is largely maintained by an increase in upflow, with the inflow and outflow strengths remaining at +/–Q_0, which leads to a much lower plateau concentration

$$C_{\max} = \frac{q_{in}C_{in}}{q_{in} + q_w} = \frac{Q_0 C_{in}}{Q_0 + Q}. \tag{3.12}$$

Hence by varying Q, we can learn something about the nature of the upflow from below. This procedure can also be applied to individual feed points, as described in the following section.

3.3 Investigating Feed-Point Nature by Analyzing FEC Logs with Two or More Q's

When wellbore FEC logging is done using a single pumping rate Q, we can determine feed-point strengths q_i by investigating $C(x)$ and $M(t)$, as described in Section 2. However, without additional information, we do not know whether differences between q_i values arise from differences in T_i or in P_i or in both (see Equation (3.1)). However, Equations (3.7) through (3.9) indicate that the change in q_i arising from a change in Q depends on how T_i and P_i differ between feed points. Thus, by repeating FEC logging using a different value of Q, we can infer more information about the feed points (as well as confirming analysis of single-Q FEC logs).

For example, if the change in feed-point strength Δq_i is the same for all feed points when Q is changed, then according to Equation (3.8), all the T_i's are the same, and differences between q_i's arise from differences between P_i's (i.e., $q_i \sim P_i$). A more common situation is for all the P_i's to be the same and for differences between q_i's to arise from differences between T_i's (i.e., $q_i \sim$

T_i). In this latter case, Equation (3.9) predicts that the relative change in feed-point strength $\Delta q_i/q_i$ will be the same for all feed points when Q is changed. If neither Δq_i nor $\Delta q_i/q_i$ are the same for all feed points, then differences between q_i's comes from differences between both T_i's and P_i's. Figure 3.5 illustrates this behavior.

In general, we can rearrange Equation (3.7) to isolate the known quantities on the left-hand-side

$$\frac{\Delta q_i}{\Delta Q} = \frac{T_i}{T_{tot}}, \tag{3.13}$$

which indicates that the fractional change in pumping rate exhibited by a feed point equals the fractional hydraulic transmissivity of the feed point. Similar information about the differences between the P_i's may be obtained as follows. We can rewrite Equation (3.2) for Q as

$$Q = \sum T_i (P_i - P_{wb}) = T_{tot}(P_{avg} - P_{wb}), \tag{3.14}$$

where P_{avg}, defined as

$$P_{avg} = \frac{\sum T_i P_i}{T_{tot}}, \tag{3.15}$$

is the hydraulic-transmissivity weighted average feed-point pressure. Rearranging Equation (3.14) yields

$$\frac{Q}{T_{tot}} = P_{avg} - P_{wb}, \tag{3.16}$$

rearranging Equation (3.1) yields

$$\frac{q_i}{T_i} = P_i - P_{wb}, \tag{3.17}$$

and taking the ratio yields

$$\frac{q_i T_{tot}}{Q T_i} = \frac{P_i - P_{wb}}{P_{avg} - P_{wb}}. \tag{3.18}$$

Eliminating T_{tot}/T_i by using Equation (3.13) gives

$$\frac{q_i / \Delta q_i}{Q / \Delta Q} = \frac{P_i - P_{wb}}{P_{avg} - P_{wb}}. \tag{3.19}$$

All the terms on the left-hand-side are known; hence, the relative pressure difference driving flow into or out of the wellbore at the *i*th feed point can be determined. Note from Equation (3.16) that when $Q = 0$, $P_{avg} = P_{wb}$. That is, P_{avg} is the pressure that would be measured in the wellbore when there is no pumping, only internal wellbore flow between feed points with different values of P_i.

Determining the values of T_i (Equation 3.13) and P_i (Equation 3.19) relative to the values of other feed points is the most information we can glean using FEC analysis itself. However, if the wellbore pressure change during FEC logging (P_{avg} - P_{wb}) is monitored, then Equation (3.16) may be used to determine T_{tot}, enabling Equation (3.13) to determine individual T_i values uniquely. If, additionally, the value of P_{wb} itself is monitored, then the P_i values may be determined from Equation (3.19). In practical field conditions, it is indeed straightforward to monitor wellbore fluid pressures.

The results from two fluid logging tests with different pumping rates potentially provide a powerful way of determining T_i and P_i values for all feed points, relative to those of one feed point. Thus, we consider two distinct feed points, *i* and *j*, write Equations (3.13) and (3.19) for each one, and take the ratio:

$$\frac{\Delta q_i}{\Delta q_j} = \frac{T_i}{T_j} \tag{3.20}$$

$$\frac{q_i / \Delta q_i}{q_j / \Delta q_j} = \frac{P_i - P_{wb}}{P_j - P_{wb}} \tag{3.21}$$

The Δq values and $q/\Delta q$ ratios on the left-hand-sides are easily identifiable in Figures 3.5b and 3.5c, respectively. In practice, if T_j and P_j are known for one feed point, say from a packer test either before or after the fluid logging, then the T_i and P_i values for all the rest of the feed points can be obtained simply from Equations (3.20) and (3.21). Note that these equations consider only two feed points at a time, as opposed to Equations (3.13) and (3.19), which include quantities that represent all the feed points (Q, ΔQ, T_{tot}, and P_{avg}), with more possibilities of introducing inaccuracies under imperfect, real-world conditions.

4. Application to Real Data

4.1 Raymond Field Site

At the Raymond field site, located in the foothills of the Sierra Nevada mountains in California, nine wells were drilled that penetrated a fractured granodiorite. The wells are 90 m deep and are cased over the upper 8 m through a sediment layer, then open below that. Many different kinds of well logs and well tests have been conducted in these wells, to develop and test equipment and methodologies for characterizing the hydrological behavior of fractured rock (Karasaki et al., 2000). Flowing wellbore electrical-conductivity logging was carried out in seven of the nine wells (Cohen, 1995) using pumping rates ranging from 7 to 20 L/min. Logging was conducted while the tool was moved up and down the wellbore. FEC profiles obtained during upward logging showed smeared-out, less well-defined peaks that are slightly offset from those obtained

during downward logging, and are not used. Six or seven downward logging profiles for increasing time were obtained for each well. Because the wells are quite shallow, borehole temperatures do not vary much with depth, and FEC values do not need to be corrected for temperature variations (see Appendix). FEC is converted to C using the quadratic relationship given in Equation (A.1). Here, we present and analyze concentration profiles from the two wells at the Raymond site, labeled SW1 and W00, that show the most interesting signatures.

Figure 4.1 shows the concentration profiles for well SW1. Six inflow points can be identified. The diffusive shape of the lower limb of the lowest peak (peak 1) suggests that $q_w = 0$. Three peaks (Peaks 2, 3, and 4) show an approach to steady state, enabling estimates of $C_{\max i}$ to be made. We ignore the shallowest peak ($x = 2 - 8$ m), which decays rather than grows, on the assumption that it is evidence of leakage around the casing rather than fracture flow. Such leakage has been confirmed by field observations (Cohen, 1995). Five of the peaks are well enough separated to use the area under the individual peaks to determine $M_i(t)$, the mass arising from the ith feed point as a function of time (Figure 4.2). We then fit a straight line to $M_i(t)$ and use Equation (2.12) to identify the slope of the line as $q_i C_i$ and the time-axis intercept as t_{0i}. In general, the late-time drop in $M_i(t)$ below the linear fitting line does not identify outflow, as described in Section 2, but indicates the peak reaching the edge of the integration domain. Note in Figure 4.1 that Peak 5 overlaps with Peaks 4 and 6 too early for the estimates of $q_5 C_5$ and t_{05} obtained from $M_5(t)$ to be reliable.

For Peak 1, the $q_1 C_1$ product is well-defined, but there is no evidence of a $C_{\max 1}$ plateau. Furthermore, the height of an isolated peak such as this is very sensitive to diffusion/dispersion strength D_0, which is unknown. Therefore, we search for C_1 and D_0 values by trial and error using the BORE II code, by comparing the observed $C(x)$ profiles for Peak 1 to simulation

results. Once C_1 and q_1 have been found, Equations (2.5) and (2.6) can be used to calculate the parameters of the upper peaks. Table 4.1 summarizes the results. Recall that since Peak 1 properties are not uniquely determined, those of all shallower peaks are uncertain too. Unfortunately, the shallow leakage around the casing precludes the use of Q to constrain the q_i values. Figure 4.3 shows $C(x)$ profiles simulated with BORE II using the parameters given in Table 4.1. The simulated profiles match the observed ones approximately, but there is room for improvement. In particular, Peak 5 is much too small and there is generally not enough interference between the upper five peaks. Because the peaks overlap relatively early, the $M_i(t)$ integrals cannot extend as far along the wellbore as they should. Thus, they tend to underestimate the q_iC_i products, which in turn leads to too-small values of q_i.

The parameter values shown in Table 4.1 are then optimized by data fitting using BORE II simulations. Figure 4.4 shows the results of this fitting process, and Table 4.2 shows the corresponding feed-point properties. Note that inflow point 4a with $C_i = C_0$ has been added between Peaks 4 and 5, to account for the narrow peak and lower plateau above Peak 4 (compare to Figure 2.4). With just this additional inflow, the upward flow through the wellbore at Peak 6 is too big (C_{max6} is too small and the peak is too broad), so we also need to add outflow point 4b just below Peak 5. Overall, the property changes required for the existing feed points are minor. Peak 5 is an exception, but examination of the $C(x)$ profiles (Figure 4.1) made it clear a priori that this peak was too close to adjacent peaks to be well characterized.

It is interesting to note, from Table 4.2, the advantages of the flowing wellbore electric-conductivity logging method. From one set of data, obtained in only about one hour (Cohen, 1995), we are able to identify the locations of eight conducting fractures intersected by the well, including one where the flow is out of the borehole to the fractures (feed point 4b in Table 4.2).

The salinity of water from the seven inflow points varies by a factor of two, except for one point that has very low salinity. Since we have the flow rates q_i for these flowing fractures, their hydraulic transmissivities can be directly calculated, using the pressure drawdown in the wellbore measured during pumping. Table 4.2 shows that variation of the hydraulic transmissivity (proportional to q_i) covers a range of almost two orders of magnitude. To obtain all this information using conventional packer methods (i.e., pump tests conducted in packed-off sections of the borehole) would require considerable more time and effort.

The second set of data from the Raymond site analyzed with our methods are from Well W00. Figure 4.5 shows the concentration profiles for this well. Five peaks are apparent. The lowest peak (Peak 1) does not show the upward skewing of a normal inflow point, but the more symmetric appearance of horizontal flow. Peaks 2 and 3 interfere after a short time. The long-time behavior of Peak 4 suggests that there is a $C_i = C_0$ inflow point above it (denoted feed point 4a) that causes a decrease from C_{max4}. We ignore the non-uniform initial condition at shallow depths, because it is likely to represent sedimentary layers and leakage around the casing.

Figure 4.6 plots $M_i(t)$ versus t for Peaks 1 and 5 individually, for Peaks 2 and 3 combined, and for Peaks 4 and 4a combined. Results are shown in Table 4.3. Because we consider Peak 1 to represent horizontal flow, which includes both inflow and outflow at the same depth, the $M_1(t)$ values obtained from the area under the peak do not directly determine the q_1C_1 product. Furthermore, because no C_{max1} plateau is visible, we need to fit q_1 and C_1 by trial and error using BORE II simulations. In contrast, for Peaks 2 and 3, we vary $q_{2,3} \equiv q_2 + q_3$ and $C_{2,3} \equiv C_2 = C_3$ while maintaining their product equal to the $q_{2,3}C_{2,3}$ value obtained from $M_{2,3}(t)$. We then vary the manner in which $q_{2,3}$ is allocated between Peak 2 and Peak 3.

For Peak 4, we initially assumed that feed point 4a contributes a negligible amount to the q_4C_4 product, because C_0 is small. However, when we used q_4 and C_4 values consistent with the q_4C_4 product given in Table 4.3 for a BORE II simulation, we got much too large a peak (profiles not shown). This suggests that the q_4C_4 product is not all associated with the feed point 4 location. If we look carefully at the early-time profiles in the vicinity of feed point 4a, we see some evidence for inflow with $C > C_0$, which would contribute to the q_4C_4 product of the combined peaks. The magnitude of the possible peak is much too small to produce a reliable estimate of the $q_{4a}C_{4a}$ product, so we proceed as follows. First, we determine q_4 and C_4 by trial and error with Bore II simulations, then multiply them to get the true value of q_4C_4, which is subtracted from the combined qC value given in Table 4.3. The remainder is $q_{4a}C_{4a}$, which is used along with C_{max4a} to determine q_{4a} and C_{4a} from Equations (2.5) and (2.6). Peak 5 is then analyzed using Equations (2.5) and (2.6). The resulting parameters are shown in Table 4.3 and the corresponding $C(x)$ profiles are shown in Figure 4.7. Above the feed point 4a, flow up the wellbore should be bigger and the early-time match for Peak 5 is not very accurate, owing to complications from the non-uniform initial conditions. Overall, however, the procedure works reasonably well. As for well SW1, additional trial-and-error parameter variations could be used in conjunction with BORE II simulations to improve the match.

Now let us examine Peak 1 more carefully. Figure 4.8 shows the same concentration profiles as Figure 4.7, but zooms in on the region around Peak 1. It is apparent that the horizontal-flow model does not capture all the features of the observed data (Figure 4.8a). If we move the outflow point a few meters below the inflow point, then the pair represents internal downward flow through the wellbore rather than horizontal flow. This feed-point configuration produces a slight downward skewing of the concentration peak at late times, consistent with the

observed data (Figure 4.8b), but it does not significantly alter the early-time concentration profiles. That is because the early-time simulated profiles reflect a short residence time in the wellbore, and the downward flow does not have time to affect them. Figure 4.6 indicates that the $M_1(t)$ data can be fit equally well by a curve as by as a straight line. Assuming a constant value of q_1, the slope of the $M_1(t)$ fitting curve determines $C_1(t)$. Using a variable $C_1(t)$ in BORE II simulations yields a better match to both early- and late-time profiles for Peak 1 (Figure 4.8c). The gradual increase in C_i implied by the nonlinear curve fit suggests a diffuse boundary between the native groundwater and the de-ionized water that entered the fracture during wellbore flushing prior to logging.

4.2 Colog Field Site

The FEC logs shown in Figure 1.1 are proprietary and the site geologic information is not made known to us. Nevertheless they provide a good example of using the mass-integral method to identify the location and strength of an outflow point. The FEC logs are converted to concentration profiles using the quadratic relationship given in Equation (A.1). Figure 4.9a shows the $C(x)$ profiles at a series of 12 times, and Figure 4.9b shows the corresponding $M(t)$ integral for the entire wellbore section from $x = 146$ to $x = 226$ m, denoted M_{226}. The first two points on the M_{226} curve essentially represent the initial conditions, so they are not included in the early-time data fit to a straight line, which yields $S_{\text{early}} = 0.081$ kg/hr and $t_0 = 0.22$ hr. The initial deviation from linearity occurs at a time $t = 1.6$ hr. According to Figure 4.9a, the concentration front at this time is at a depth of $x = 212$ m, which is inferred to be the outflow-point location, denoted x_{out}. Fitting the subsequent data to a straight line yields $S_{\text{late}} = 0.059$ kg/hr. Note that after a time of $t = 2.6$ hr, the concentration profiles do not show complete peaks,

so subsequent points are not included in the fit. Taking the C_{max} value at t = 2.6 hr as 0.69 kg/m^3 in Equation (2.16), an outflow strength q_{out} = 0.029 m^3/hr = 0.49 L/min is obtained.

An alternative procedure to determine q_{out} involves correcting the mass integrals to account for the fact that the limits of integration (x_1 and x_2) do not include the entire concentration peaks (Tsang et al., 1990). For the present case, when flow is downward, $M_{226}(t) = M_{x_2}(t)$ can be corrected by adding the ion mass that has flowed through the lower limit of integration, x_2, in a time t:

$$M'_{x_2}(t) = M_{x_2}(t) + q_{x_2}\int_0^t C(x_2, t')dt', \tag{4.1}$$

$$M'_{x_2}(t) = \pi r^2 \int_{x_1}^{x_2} C(x,t)dx + q_{x_2}\int_0^t C(x_2, t')dt', \tag{4.2}$$

where q_{x_2} is the volumetric flow rate down the wellbore at x_2. The left-hand-side can be represented by the late-time linear fit to $M_{x_2}(t)$, with slope S_{late}. The space and time integrals on the right-hand-side can be obtained from the concentration profiles, leaving q_{x_2} as the only unknown. A practical procedure to determine q_{x_2} is to plot both sides of the equation as a function of time and vary q_{x_2} until the concentration data show a linear trend with a slope of S_{late} for all late times (Figure 4.9c). The result is q_{226} = 0.75 L/min. This procedure can be repeated at the location of the outflow point by replacing x_2 with x_{out} in Equation (4.1):

$$M'_{x_{out}}(t) = M_{x_{out}}(t) + q_{x_{out}}\int_0^t C(x_{out}, t')dt', \tag{4.3}$$

where $q_{x_{out}}$ is the flow down the wellbore just above x_{out}. Figure 4.9b shows $M_{x_{out}}(t)$, denoted as M_{212}. Since M_{212} is identical to M_{226} at early times, we use the early-time linear fit to $M_{226}(t)$ with slope S_{early} for the left-hand-side of Equation (4.3). Plotting both sides of Equation (4.3)

and adjusting $q_{x_{out}}$ until they match (Figure 4.9c), we obtain q_{212} = 1.25 L/min. The feed-point strength q_{out} is the difference between the wellbore flow rates above and below x_{out}: $q_{out} = q_{212} - q_{226}$ = 1.25 – 0.75 = 0.50 L/min.

In the present case, the two procedures for determining q_{out} agree well because concentration at the outlet point reaches a constant C_{max} value. The latter method can be used even when this is not the case. The determination of q_{212} with Equation (4.4) would be unchanged. The determination of q_{226} with Equation (4.3) would be complicated by the fact that S_{late} would not be known, so the left-hand-side of Equation (4.3) would be undetermined, although it would still be a straight line. Thus, q_{226} would be inferred as the value that yields some straight line for the right-hand-side of Equation (4.3), rather than a particular straight line with a known slope S_{late}. This necessarily makes the matching procedure less precise, but it remains useful for providing initial guesses for numerical analysis with BORE II.

Analysis of the remaining features of the $C(x)$ profiles shown in Figure 1.1 (multiple inflow points, including an inflow point with $C = C_0$, downflow out the bottom of the logged wellbore section, and a non-uniform initial condition), as well as a numerical analysis with BORE II, are presented elsewhere (Doughty and Tsang, 2000).

5. Summary and Conclusions

Flowing wellbore electrical conductivity logging is a practical method for hydrologic characterization of individual fractures, fracture zones, or permeable layers intersecting a borehole. The first step in the analysis of a complex FEC log is to identify signatures of various flow conditions, which can greatly expedite setting up the numerical model of the borehole/fracture system used to simulate conductivity logging. For each feed point along the

borehole, we seek to identify a location, flow rate, and (for inflow points) concentration or salinity. Inflow points generally produce distinctive signatures in the concentration profiles $C(x)$ obtained directly from the FEC logs for the range of conditions discussed in this paper. These are summarized in Figure 5.1. Both early- and late-time $C(x)$ profiles provide information on inflow points, and special conditions such as time-varying flow rate or concentration can be identified. In contrast, outflow points often do not manifest themselves clearly in $C(x)$ profiles, requiring a more elaborate mass-integral analysis, in which $C(x)$ profiles are integrated over the entire borehole length to produce the ion mass in place, or mass integral, at a given time, $M(t)$. $M(t)$ is then plotted as a function of time, and breaks in slope of $M(t)$ are used to identify outflow points. These are also shown in Figure 5.1, lower right.

An understanding of the signatures produced by various flow conditions allows us to make the following recommendations concerning the operation and analysis of flowing wellbore electrical-conductivity logging:

1. Start logging as soon as possible after de-ionized water is emplaced and pumping begins, to enable the area under individual peaks to be unambiguously determined.
2. If possible, continue logging long enough for steady-state conditions to develop. Concentration plateaus for isolated peaks ($C_{\mathrm{mid}i}$) and interfering peaks ($C_{\mathrm{max}i}$) may be used with mixing rules to determine individual feed-point flow rates and concentrations.
3. Repeat logging several times with one or two other pumping rates (e.g., half and double the original pumping rate). The manner in which FEC peaks change with Q provides information not only on the flow rate of the feed points, but on the transmissivity and far-field pressure conditions of the fractures or permeable layers.

4. Packing off the bottom of the wellbore interval being studied (i.e., setting $q_w = 0$) reduces uncertainty for most analyses. However, for certain features, such as the decreasing feed-point concentration illustrated in Figure 2.3d, the presence of q_w enhances the signature.
5. For the analysis of horizontal flow, the initial series of logging runs should be done with as low a pumping rate as possible (or zero rate), to enable visual identification of the non-skewed peaks indicating horizontal flow Q_0. Subsequent logging with a relatively large pumping rate (at least $2Q_0$) encourages a C_{max} plateau to develop, which in turn enables an improved estimate of Q_0 to be made. Comparison to the Drost et al. (1968) analytical solution (for thick layers) or BORE II results (for thin layers or individual fractures) can further constrain Q_0.

A suggested step-by-step guideline for the analysis of flowing wellbore FEC logs is shown in Tables 5.1–5.5, comprising five categories: early-time analysis, late-time analysis, $M(t)$ analysis, multiple-Q analysis, and BORE II analysis. These tables also form a concise summary of all key methods presented in this paper. Generally, the recommended procedure involves first investigating inflow points in $C(x)$, using the area under individual peaks and plateau concentrations. Next, check for outflow by calculating $M(t)$ over the entire profile and examining the breaks in slope. Then, logs with different pumping rates can be taken to infer more about feed-point properties. All of these steps can be carried out in conjunction with numerical simulations using BORE II, which is also used to optimize or refine the feed-point flow rates and salinities. Finally, inferred properties should be critically evaluated in the context of other geological, hydrological, geophysical, and geochemical analyses available for the site. Such systematic studies of flowing wellbore FEC logs not only yield parameter values for

hydraulic properties of fractures or permeable layers, but also provide insight into the physical and chemical processes that have occurred.

Appendix: Governing Equations

The principal equation governing wellbore FEC variation is the one-dimensional advection-diffusion equation for the transport of mass (or ion concentration) in the wellbore. However, additional consideration must be given to the determination of FEC as a function of ion concentration and the temperature dependence of FEC.

A.1 FEC as a Function of Concentration

The relationship between ion concentration and FEC is reviewed, for example, by Shedlovsky and Shedlovsky (1971), who give graphs and tables relating these two quantities. Hale and Tsang (1988) made a sample fit for the case of NaCl solution at low concentrations and obtained

$$\mathrm{FEC} = 1{,}870\, C - 40\, C^2, \qquad \text{(A.1)}$$

where C is ion concentration in kg/m^3 ($\approx$ g/L) and FEC is in μS/cm at 20°C. The expression is accurate for a range of C up to $\approx$ 6 kg/m^3 and FEC up to 11,000 μS/cm. The quadratic term can be dropped if we are interested only in values of C up to $\approx$ 4 kg/m^3 and FEC up to 7,000 μS/cm, in which case the error will be less than 10%.

Fracture fluids typically contain a variety of ions, the most common being Na^+, Ca^{2+}, Mg^{2+}, Cl^-, SO_4^{2-}, and HCO_3^-. If a hydrochemical analysis has been completed, various methods are available for computing an equivalent NaCl concentration for other ions. Schlumberger (1984) presents charts of multiplicative factors that convert various solutes to equivalent NaCl concentrations with respect to their effect on FEC.

A.2 Temperature Dependence of FEC

In the present work, calculations are made assuming a uniform temperature throughout the wellbore. Actual wellbore temperatures generally vary with depth, so temperature corrections must be applied to field FEC data to permit direct comparison with model output.

The effect of temperature T on FEC can be estimated using the following equation (Schlumberger, 1984):

$$\mathrm{FEC}(20^{\circ}\,\mathrm{C}) = \frac{\mathrm{FEC}(T)}{1 + S(T - 20^{\circ}\,\mathrm{C})}, \tag{A.2}$$

where $S = 0.024$.

Generally, temperature increases with depth below the land surface. If complete temperature logs are available, these data can be used to correct the corresponding FEC values. However, if complete logs are not available, the temperature variation in the wellbore can often be approximated as linear:

$$T = Ax + B, \tag{A.3}$$

where A and B are parameters determined by fitting any available temperature versus depth data at the site. If the fit is unsatisfactory, relationships with higher-order terms may be used.

A.3 Advection-Diffusion Equation

The advection-diffusion equation describes the evolution of ion concentration as a function of space and time in a wellbore containing multiple feed points, given the pumping rate of the well, the inflow or outflow rate of each feed point, its location, and, for inflow points, its ion concentration. We assume that transport occurs by longitudinal advection and diffusion along the wellbore, with instantaneous mixing of feed-point fluid in the plane of the wellbore cross

section. These assumptions allow use of a one-dimensional model; the differential equation for mass or solute transport in a wellbore is:

$$\frac{\partial}{\partial x}\left(D_o \frac{\partial C}{\partial x}\right) - \frac{\partial}{\partial x}(Cv) + S = \frac{\partial C}{\partial t}, \qquad \text{(A.4)}$$

where x is depth, t is time, and C is ion concentration. The first term is the diffusion term, with D_0 the diffusion/dispersion coefficient in m^2/s, the second term is the advective term, with v the fluid velocity in m/s, and S is the source term in kg/m^3s. This one-dimensional partial differential equation is solved numerically using the finite-difference method, with upstream weighting applied in the advective term. The following initial and boundary conditions are specified:

$C(x, 0) = C_0(x)$, (A.5)

$C(x_{min}, t) = C_0(x_{min})$ for flow into the wellbore from above,

$C(x_{max}, t) = C_0(x_{max})$ for flow into the wellbore from below,

$D_0 = 0$ for $x < x_{min}$ and $x > x_{max}$.

The first condition allows for the specification of initial ion concentrations in the wellbore. The second and third conditions allow for advective flow of ions into the wellbore interval from above and below. The final condition ensures that diffusion and dispersion do not take place across the boundaries of the wellbore interval. In general, advection will be the dominant process at the boundaries. If diffusion or dispersion is dominant for a particular problem, the boundaries should be extended to prevent improper trapping of electrolyte.

Acknowledgments

Discussions with Stratis Vomvoris of NAGRA, Switzerland, at the initial stage of this work were appreciated. We thank him and Kenzi Karasaki and Rob Trautz of Lawrence

Berkeley National Laboratory (LBNL) for carefully reviewing this paper. We are also grateful to K. Karasaki of LBNL and G. Bauer of Colog, Inc. for making their sample data sets available to us. This work was jointly supported by the Underground Injection Control Program, Office of Ground Water and Drinking Water, U.S. Environmental Protection Agency and by the Japan Nuclear Cycle Research Institute (JNC) under a binational agreement between JNC and U.S. Department of Energy (DOE), Office of Environmental Management, Office of Science and Technology, under DOE contract DE-AC03-76SF00098.

References

Cohen, A.J.B., Hydrogeologic characterization of fractured rock formations: A guide for groundwater remediators, *Rep. LBL-38142*, Lawrence Berkeley National Laboratory, Berkeley, CA, 1995.

Doughty, C. and C.-F. Tsang, BORE II – A code to compute dynamic wellbore electrical conductivity logs with multiple inflow/outflow points including the effects of horizontal flow across the well, *Rep. LBL-46833,* Lawrence Berkeley National Laboratory, Berkeley, CA, 2000.

Drost, W., D. Klotz, A. Koch, H. Moser, F. Neumaier, and W. Rauert, Point dilution methods of investigating ground water flow by means of radioisotopes, *Water Resources Res.*, 4(1), 125-146, 1968.

Hale, F.V. and C.-F. Tsang, A code to compute borehole conductivity profiles from multiple feed points, *Rep. LBL-24928*, Lawrence Berkeley Laboratory, Berkeley, Calif., 1988.

Karasaki, K., B. Freifeld, A. Cohen, K. Grossenbacher, P. Cook, and D. Vasco, A multidisciplinary fractured rock characterization study at Raymond field site, Raymond, CA, *J. of Hydrology*, 236, 17-34, 2000

Loew, S., C.-F. Tsang, F.V. Hale, and P. Hufschmied, The application of moment methods to the analysis of fluid electrical conductivity logs in boreholes, *Rep. LBL-28809*, Lawrence Berkeley Laboratory, Berkeley, CA, 1990.

Schlumberger, Ltd., Log interpretation charts, New York, 1984.

Shedlovsky, T. and L. Shedlovsky, Conductometry, in *Physical Methods of Chemistry, Part IIA: Electrochemical Methods*, edited by A. Weissberger and B.W. Rossiter, pp. 164-171, Wiley-Interscience, New York, 1971.

Tsang, C.-F. and F. V. Hale, A direct integral method for the analysis of borehole fluid conductivity logs to determine fracture inflow parameters, Proceedings of the National Water Well Conference on New Field Techniques for Quantifying the Physical and Chemical Properties of Heterogeneous Aquifers, Dallas, Texas, March 20-23, 1989, *Rep. LBL-27930*, Lawrence Berkeley Laboratory, Berkeley, CA, 1989.

Tsang, C.-F., P. Hufschmeid, and F.V. Hale, Determination of fracture inflow parameters with a borehole fluid conductivity logging method, *Water Resources Res.*, 26(4), 561-578, 1990.

Figure Captions

Figure 1.1. Example of flowing wellbore FEC logs (Colog, Inc., personal communication, 1999). Later profiles are shown as thicker lines.

Figure 2.1. Simulated concentration profiles for three inflow feed points: (a) at early times before peaks interfere; and (b) at later times, including near steady-state conditions.

Figure 2.2. Simulated concentration profiles for three inflow feed points with the addition of upflow from below: (a) at early times before peaks interfere; and (b) at later times, including steady-state conditions.

Figure 2.3. Simulated concentration profiles obtained at early times for inflow points with (a) constant C_i; (b) increasing C_i; (c) decreasing C_i; and (d) decreasing C_i and upflow from below. The profiles are equally spaced in time.

Figure 2.4. Simulated concentration profiles for an inflow point with $C_i = C_0$ (a) above another inflow point; (b) above another inflow point with upflow from below; (c) above another inflow point at long times; and (d) below another inflow point. On each plot, the profiles are equally spaced in time.

Figure 2.5. Simulated concentration profiles obtained at early times for an outflow point (a) below another inflow point; (b) below another inflow point with upflow from below; (c) above another inflow point; and (d) above another inflow point with upflow from below. The profiles are equally spaced in time.

Figure 2.6. Simulated concentration profiles obtained at long times for widely separated inflow and outflow points.

Figure 2.7. Simulated concentration profiles comparing inflow and horizontal flow for (a) a single inflow point; (b) a thin layer of horizontal flow; (c) a single inflow point with little

longitudinal diffusion; (d) a thin layer of horizontal flow with little longitudinal diffusion; (e) a thick inflow zone; and (f) a thick layer of horizontal flow and the Drost et al. (1968) analytical solution (symbols). The time interval doubles between successive concentration profiles.

Figure 2.8. Simulated concentration versus time curves for the horizontal-flow cases shown in Figure 2.7b, d, and f, as well as for a thick layer with little longitudinal diffusion and the Drost et al. (1968) analytical solution.

Figure 2.9. Short-time example of the mass-integral method: (a) simulated concentration profiles; and (b) $M(t)$ integral and linear fit to early points.

Figure 2.10. Long-time example of the mass-integral method: (a) simulated concentration profiles; and (b) $M(t)$ integral and linear fits to early and late points.

Figure 3.1. The effect of varying Q on concentration profiles for a single inflow point. On each plot, the profiles are equally spaced in time.

Figure 3.2. The effect of varying Q on concentration profiles and mass integral for inflow and outflow points when all T_i's are the same.

Figure 3.3. The effect of varying Q on concentration profiles for horizontal flow Q_0: (a) $Q = 0$; (b) $Q = Q_0/2$; (c) $Q = Q_0$; and (d) $Q = 2Q_0$. The profiles are equally spaced in time.

Figure 3.4. The effect of varying Q on concentration profiles for horizontal flow Q_0 when upflow is present: (a) and (b) $Q = Q_0/2$; (c) and (d) $Q = Q_0$; (e) and (f) $Q = 2Q_0$. In the left column, upflow is from one inflow point; in the right column, upflow is from an extensive recharge zone. The profiles are equally spaced in time.

Figure 3.5. The effect of varying Q on inflow rates q_i: (a) inflow rates for base Q and doubled Q; (b) Δq for each feed point (feed points with the same Δq_i have the same T_i); (c) $\Delta q/q$ for each feed point (feed points with the same $\Delta q/q$ have the same P_i).

Figure 4.1. Concentration profiles obtained from wellbore electrical conductivity logging of well SW1 at the Raymond field site in California (K. Karasaki, personal communication, 2001; see also Karasaki et al., 2000). Equation (A.1) is used to convert FEC to C. Concentration profile times (in minutes) are 1.8, 14, 25, 39, 52, and 66, with later profiles shown as thicker lines. The vertical arrows identify feed-point locations and the horizontal arrows indicate the integration range for the corresponding peak.

Figure 4.2. Mass integrals $M_i(t)$ for the six concentration peaks shown in Figure 4.1 and the linear fits used to determine q_iC_i (slope) and t_{0i} (time-axis intercept).

Figure 4.3. Comparison of observed and simulated concentration profiles for Raymond well SW1 for the initial parameter set (Table 4.1), obtained by analysis of observed concentration profile signatures.

Figure 4.4. Comparison of observed and simulated concentration profiles for Raymond well SW1 for the final parameter set (Table 4.2), obtained by trial-and-error fitting with BORE II.

Figure 4.5. Concentration profiles obtained from wellbore electrical-conductivity logging of well W00 at the Raymond field site in California (K. Karasaki, personal communication, 2000). Equation (A.1) is used to convert FEC to C. Concentration profile times (in minutes) are 3.5, 15, 26, 38, 51, 62, and 99, with later profiles shown as thicker lines. The vertical arrows identify feed-point locations and the horizontal arrows indicate the integration range for the corresponding peak.

Figure 4.6. Mass integrals $M_i(t)$ for four of the concentration peaks shown in Figure 4.5 and the linear fits used to determine q_iC_i (slope) and t_{0i} (time-axis intercept). For Peak 1, the cubic curve fit to $M_1(t)$ (dashed line) may be used to determine a time-dependent C_1.

Figure 4.7. Comparison of observed and simulated concentration profiles for Raymond well W00 for the parameter set (Table 4.3) obtained by analysis of observed concentration profile signatures.

Figure 4.8. Comparison of observed and simulated concentration profiles for the lowest peak of Raymond well W00: (a) horizontal flow; (b) inflow with constant C_1 above outflow; and (c) inflow with variable $C_1(t)$ (see Figure 4.6) above outflow.

Figure 4.9. Use of the mass-integral method to identify an outflow point: (a) $C(x)$ profiles; (b) $M(t)$ integral for the entire wellbore section (M_{226}) along with linear fits to early and late points, and $M(t)$ integral for the wellbore section above the outflow point (M_{212}); and (c) corrected $M(t)$ integrals for the entire wellbore section (M_{226}') and for the section above the outflow point (M_{212}'). The lines show the linear fits used for the left-hand-sides of Equations (4.3) and (4.4) and the symbols show the right-hand-sides incorporating the optimal values of q_{226} and q_{212}.

Figure 5.1. Overview of the $C(x)$ and $M(t)$ signatures discussed in this paper, along with the section number where each is presented.

Tables

Table 2.1. Feed-point parameters inferred from concentration profiles shown in Figure 2.1. The actual feed-point parameters used to generate the concentration profiles are shown in parentheses if they differ from the inferred values. The differences reflect numerical inaccuracies in integration and estimation procedures.

Parameter	**How Determined**	**Feed Point**		
		1	2	3
x (m)	Observed from early-time $C(x)$ profiles	120	90	60
qC (kg/s)	Calculated from area under early-time $C(x)$ peak	3.79E-6 (3.75E-6)	7.70E-6 (7.50E-6)	1.16E-5 (1.13E-5)
C_{max} (kg/m^3)	Observed from late-time $C(x)$ profiles	0.30	0.45	0.60
q (m^3/s)	Calculated from current C_{max} and current and deeper qC values	1.26E-5 (1.25E-5)	1.29E-5 (1.25E-5)	1.29E-5 (1.25E-5)
C (kg/m^3)	Calculated from current qC and q values	0.30	0.60	0.89 (0.90)

Table 4.1. Parameters estimated for Raymond Site Well SW1 using analysis of concentration profile signatures (corresponding $C(x)$ profiles are shown in Figure 4.3).

Parameter	**How Determined**	**Feed Point**					
		1	2	3	4	5	6
x (m)	Observed from early-time $C(x)$ profiles	64	36	28	22	16	14
qC (g/min)	Calculated from area under early-time $C(x)$ peak	0.21	0.007	0.009	0.042	0.0010	0.042
C_{max} (g/L)	Estimated from late-time $C(x)$ profiles	0.11*,[a]	0.008	0.012	0.029*	0.024*	0.038*
q (L/min)	Calculated from current C_{max} and current and deeper qC values	2.1[a]	0.058	0.062	0.21	0.011	0.200
C (g/L)	Calculated from qC and q values	0.11	0.13	0.15	0.21	0.13	0.21

*Not well constrained by $C(x)$ profile, estimated in conjunction with q and C.
[a]Determined by trial and error using BORE II

Table 4.2. Final parameter set for Raymond Site Well SW1, obtained by varying the parameters given in Table 4.1 as needed for BORE II simulations to match observed data (corresponding $C(x)$ profiles are shown in Figure 4.4).

Parameter	**Feed Point**							
	1	2	3	4	4a	4b	5	6
x (m)	64	36	28	22	20	17	16	14
q (L/min)	2.1	0.058	0.070	0.25	0.60	–1.0	0.057	0.20
C (g/L)	0.11	0.13	0.15	0.21	0.0050	N/A	0.20	0.22

Table 4.3. Summary of parameters for Raymond well W00. Corresponding $C(x)$ profiles are shown in Figure 4.7.

Parameter	**How Determined**	**Feed Point**					
		1	2	3	4	4a	5
x (m)	Observed from early-time $C(x)$ profiles	72	61	58	29	26	12
qC (g/min)	Calculated from area under early-time $C(x)$ peak	0.055	0.27		0.62		0.11
C_{max} (g/L)	Estimated from late-time $C(x)$ profiles	0.25*	0.12*		0.084	0.079	0.085*
q (L/min)	Determine by trial and error using BORE II	+/–0.25[b]	1.6	0.66	2.4	3.2	0.72
C (g/L)	Calculated from qC and q values	0.25[b]	0.12	0.12	0.16	0.072	0.15

*Not well constrained by $C(x)$ profile, estimated in conjunction with q and C.
[b]Horizontal flow, q and C determined by trial and error independent of the qC product obtained from area under peak

Table 5.1. Step-by-step guide to analysis of flowing wellbore FEC logs: early-time analysis.

Table 5.2. Step-by-step guide to analysis of flowing wellbore FEC logs: late-time analysis.

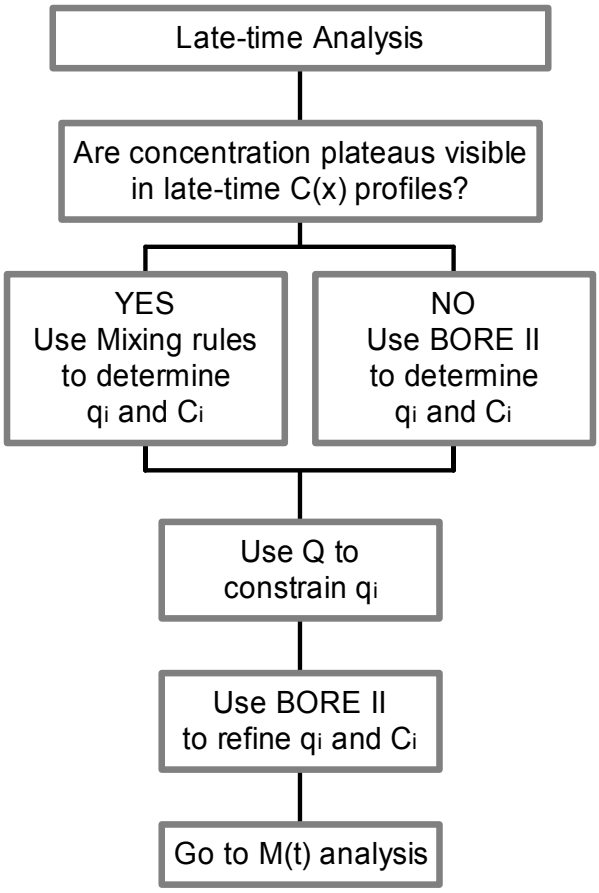

Table 5.3. Step-by-step guide to analysis of flowing wellbore FEC logs: mass-integral $M(t)$ analysis.

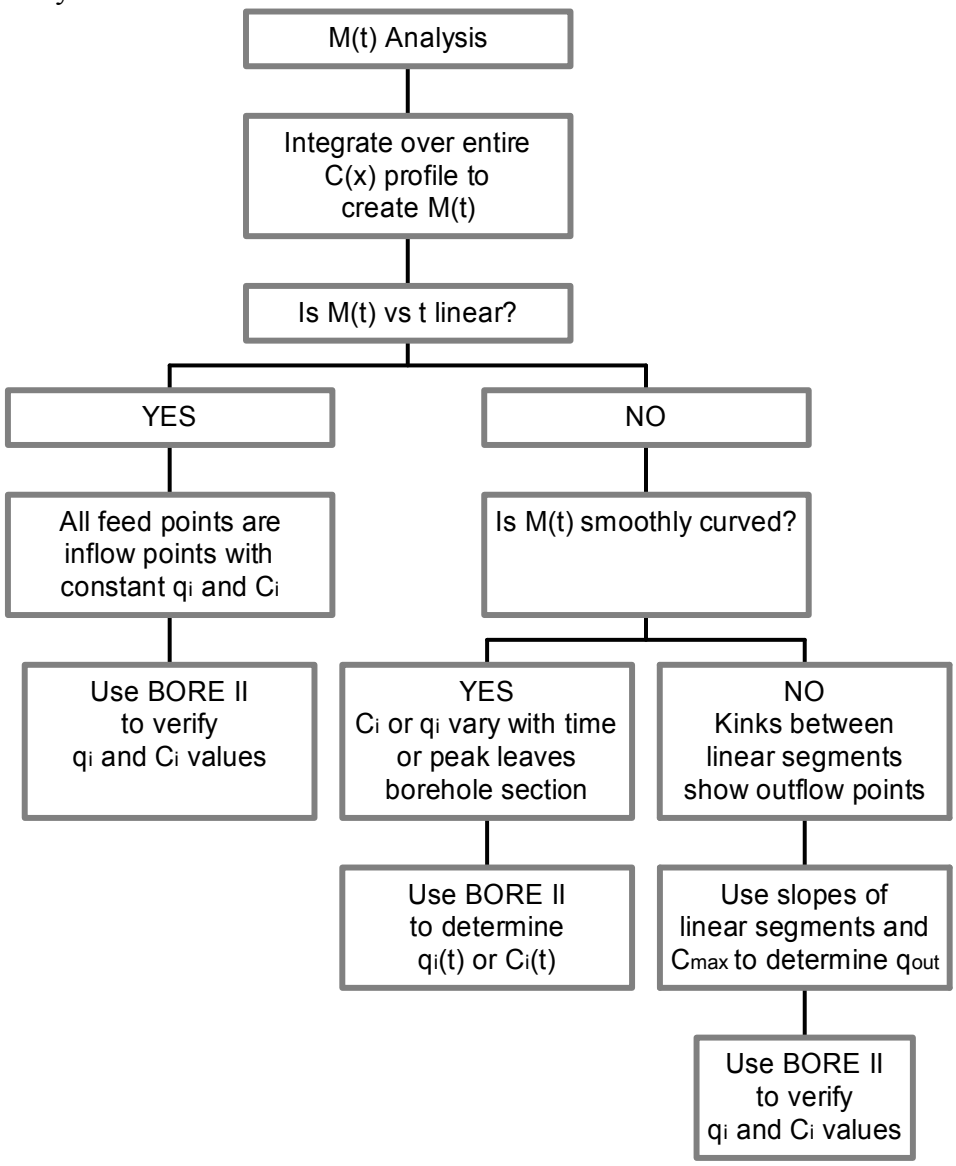

Table 5.4. Step-by-step guide to analysis of flowing wellbore FEC logs: analysis of logs with two or more *Q*'s.

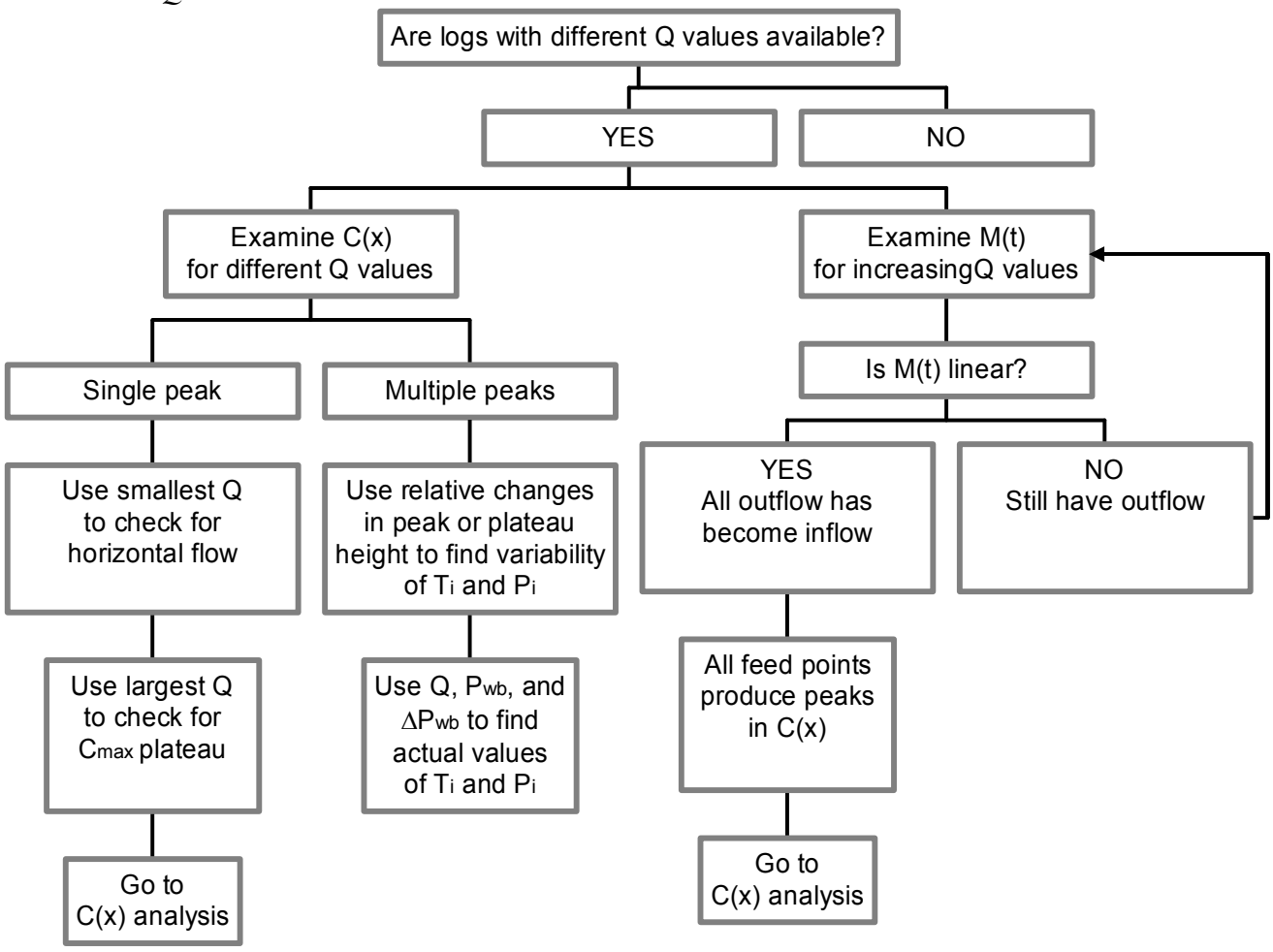

Table 5.5. Step-by-step guide to analysis of flowing wellbore FEC logs: BORE II analysis.

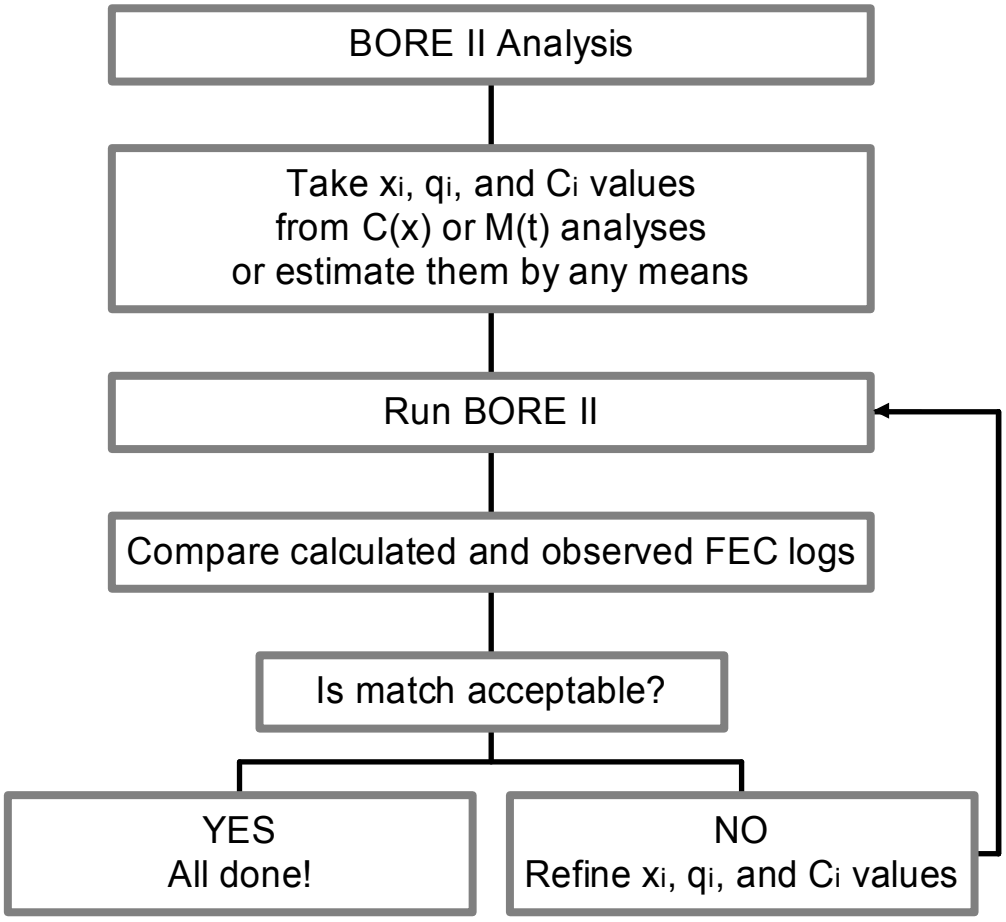

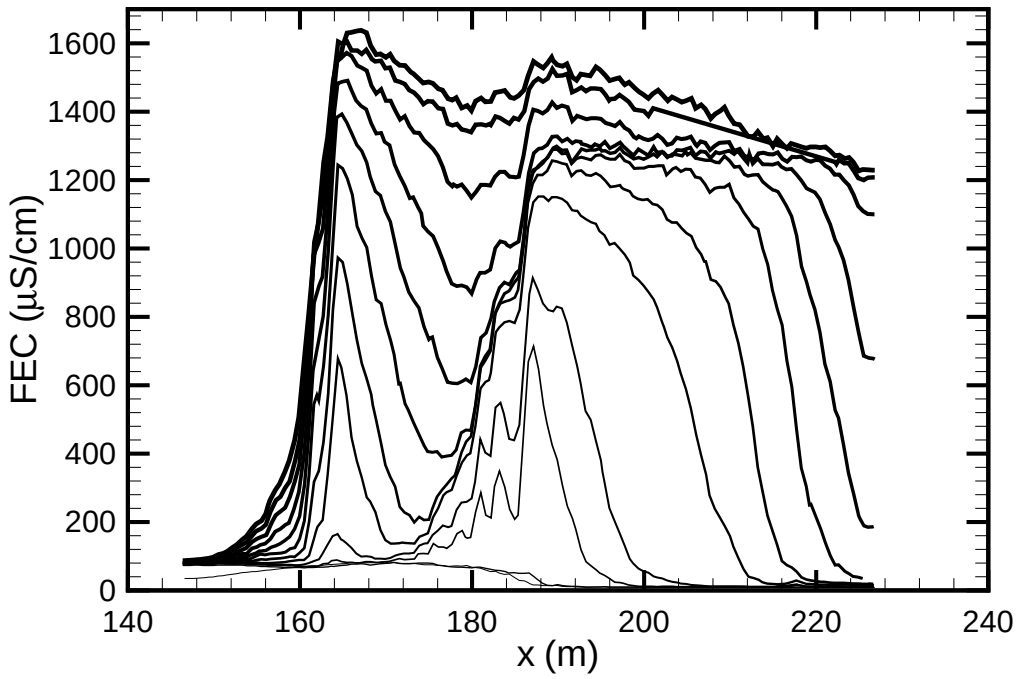

Figure 1.1. Example of flowing borehole FEC logs (Colog, Inc., personal communication, 1999). Later profiles are shown as thicker lines.

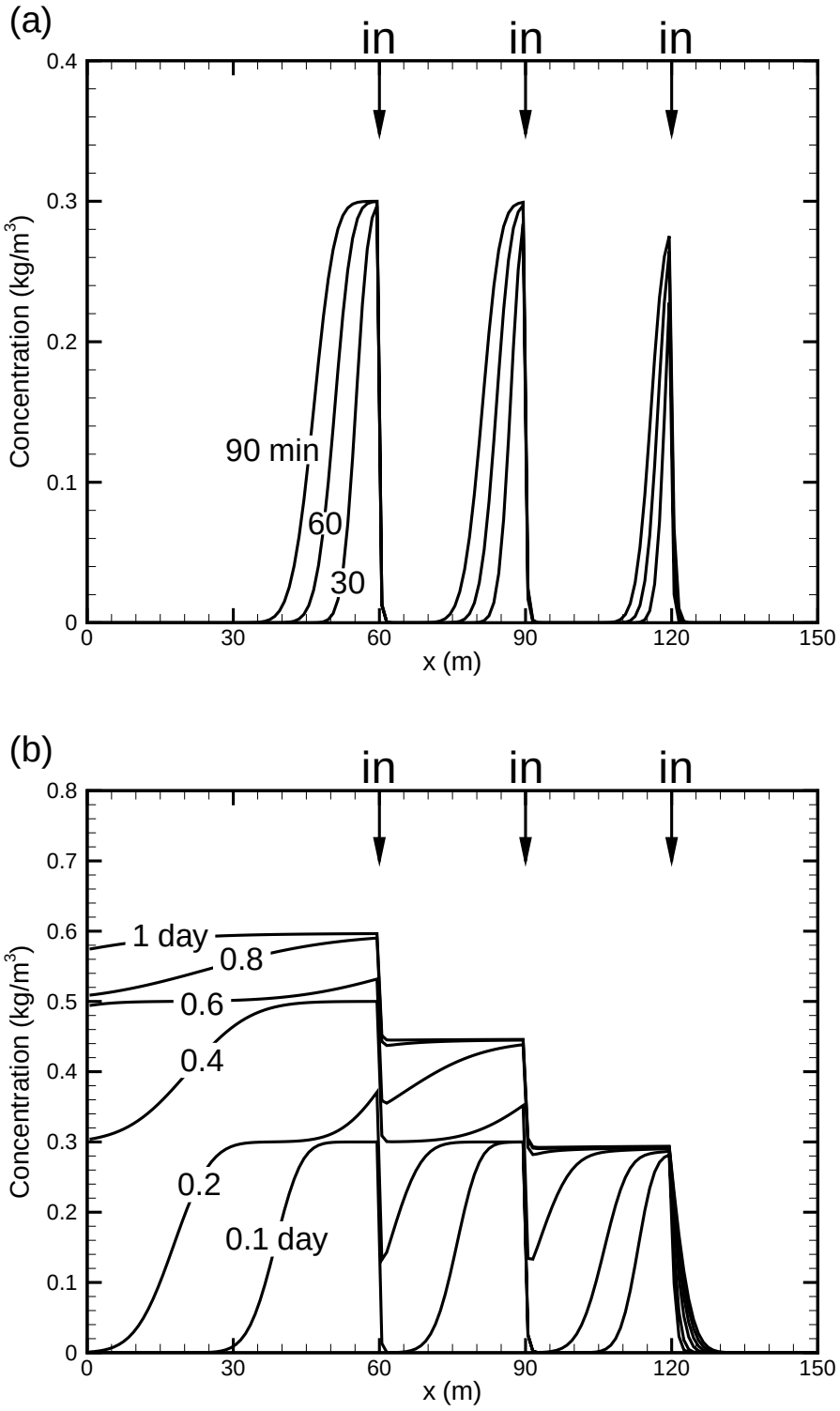

Figure 2.1. Simulated concentration profiles for three inflow feed points: (a) at early times before peaks interfere; and (b) at later times, including near steady-state conditions.

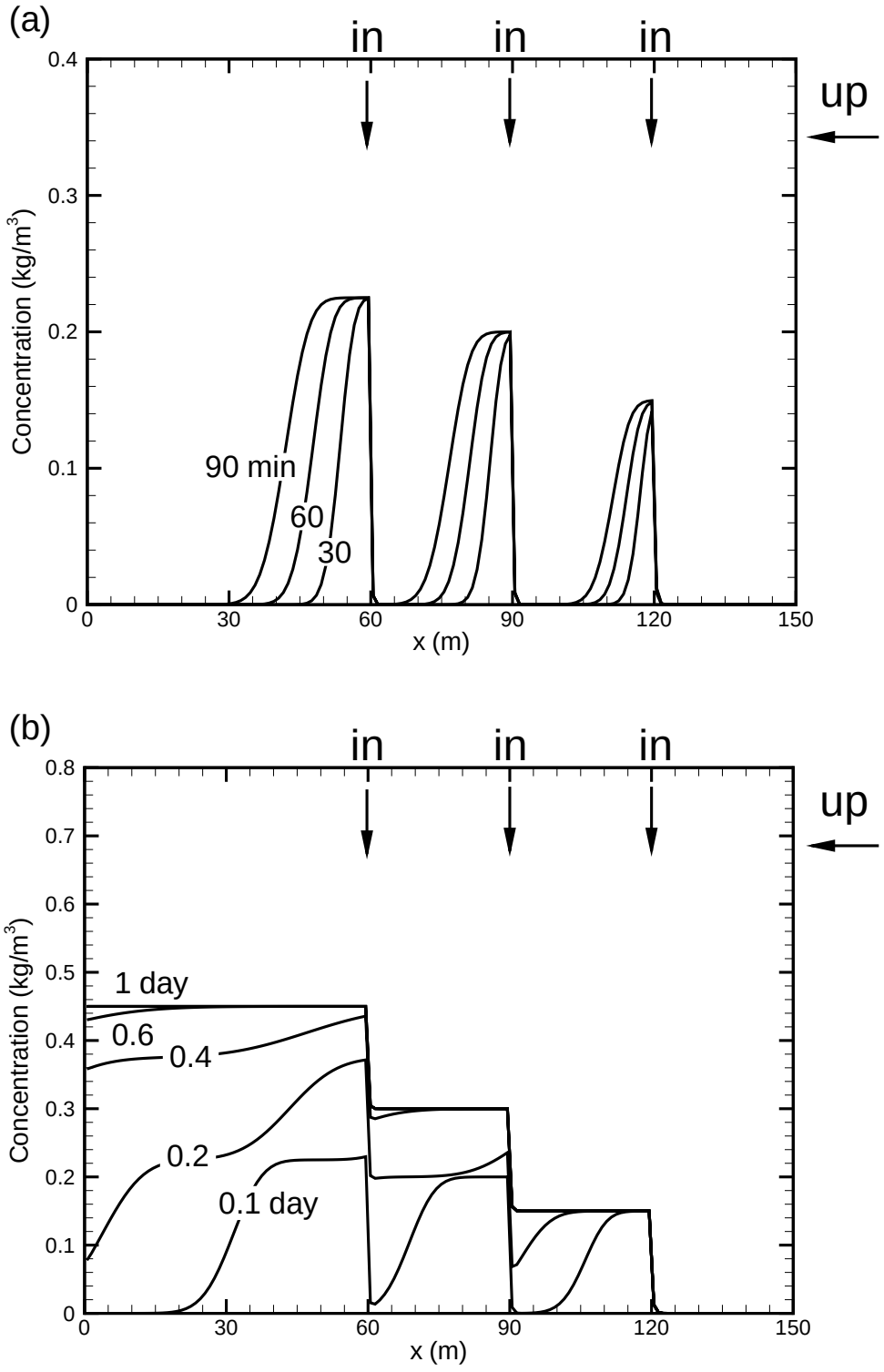

Figure 2.2. Simulated concentration profiles for three inflow feed points with the addition of upflow from below: (a) at early times before peaks interfere; and (b) at later times, including steady-state conditions.

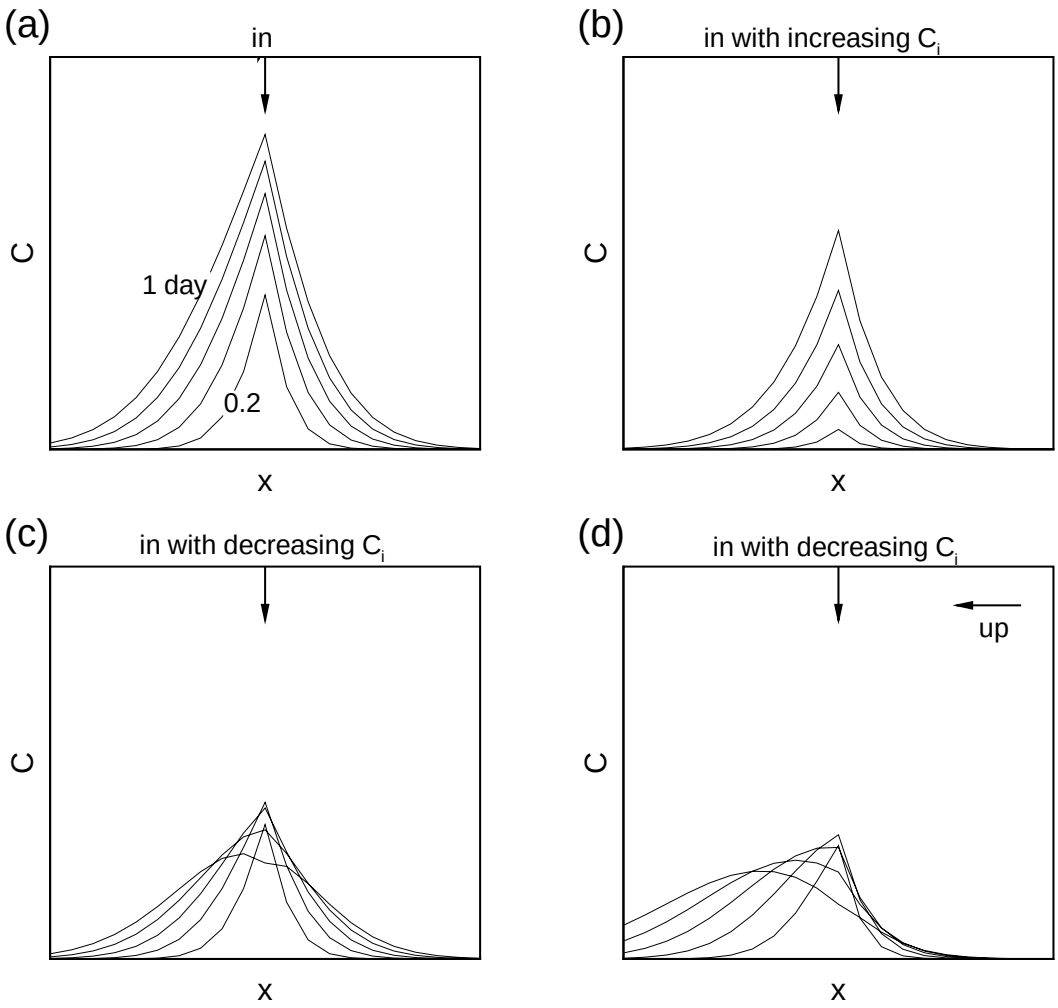

Figure 2.3. Simulated concentration profiles obtained at early times for inflow points with (a) constant C_i; (b) increasing C_i; (c) decreasing C_i; and (d) decreasing C_i and upflow from below. The profiles are equally spaced in time.

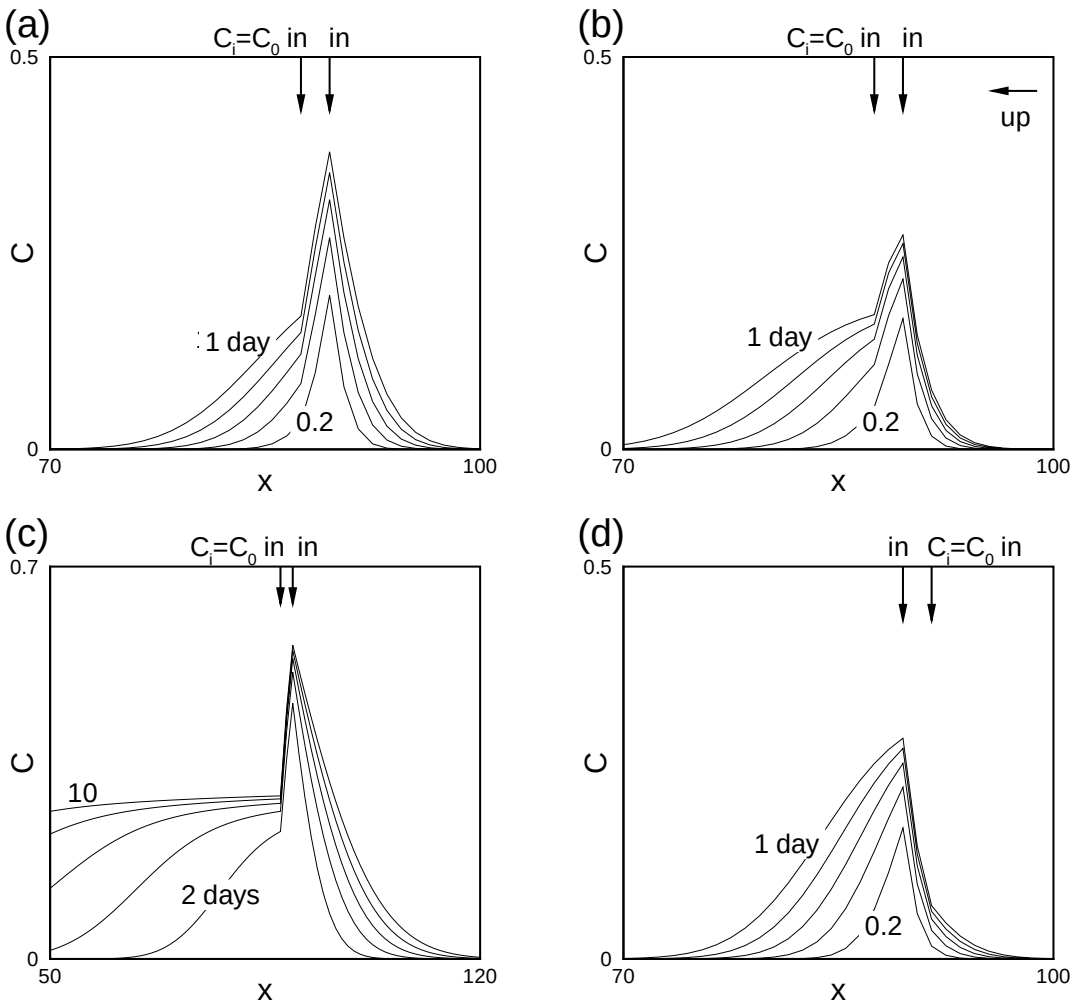

Figure 2.4. Simulated concentration profiles for an inflow point with $C_i = C_0$ (a) above another inflow point; (b) above another inflow point with upflow from below; (c) above another inflow point at long times; and (d) below another inflow point. On each plot, the profiles are equally spaced in time.

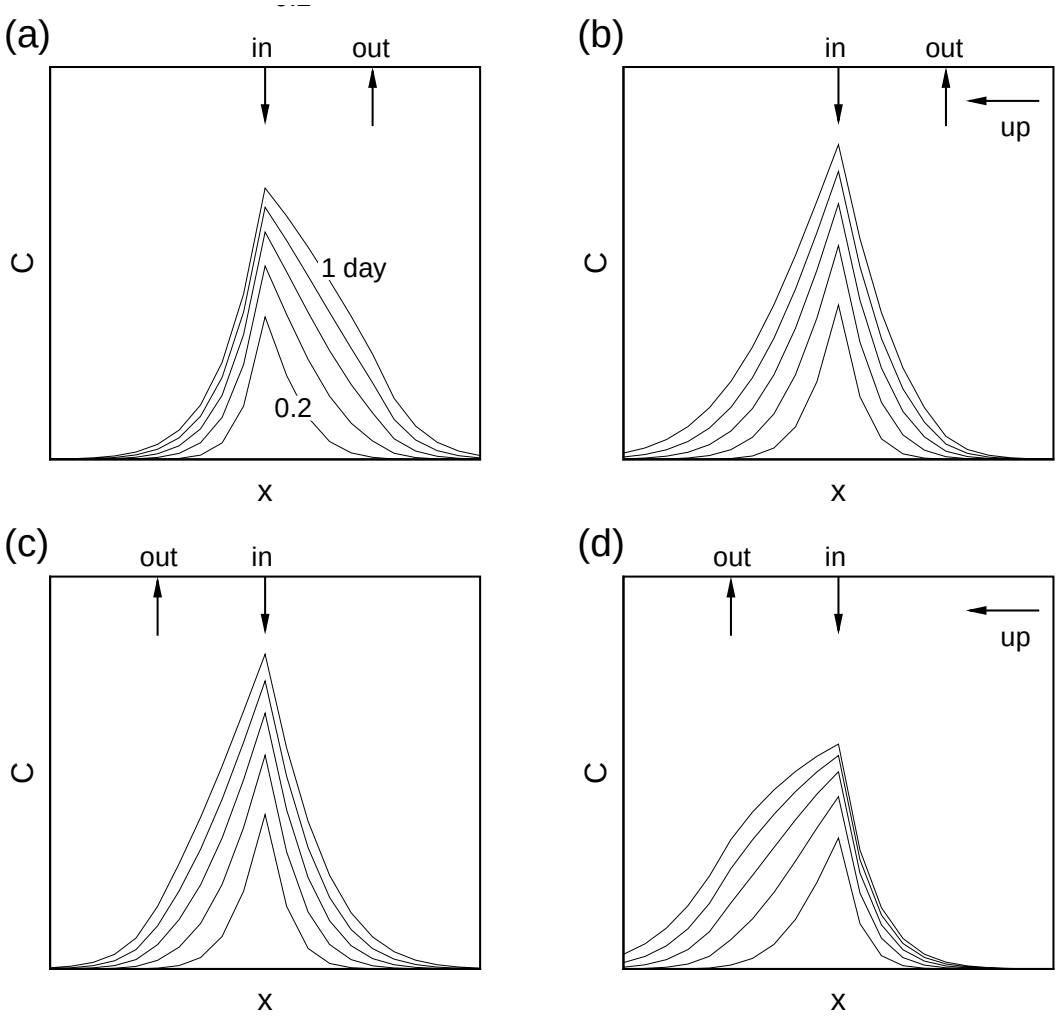

Figure 2.5. Simulated concentration profiles obtained at early times for an outflow point (a) below another inflow point; (b) below another inflow point with upflow from below; (c) above another inflow point; and (d) above another inflow point with upflow from below. The profiles are equally spaced in time.

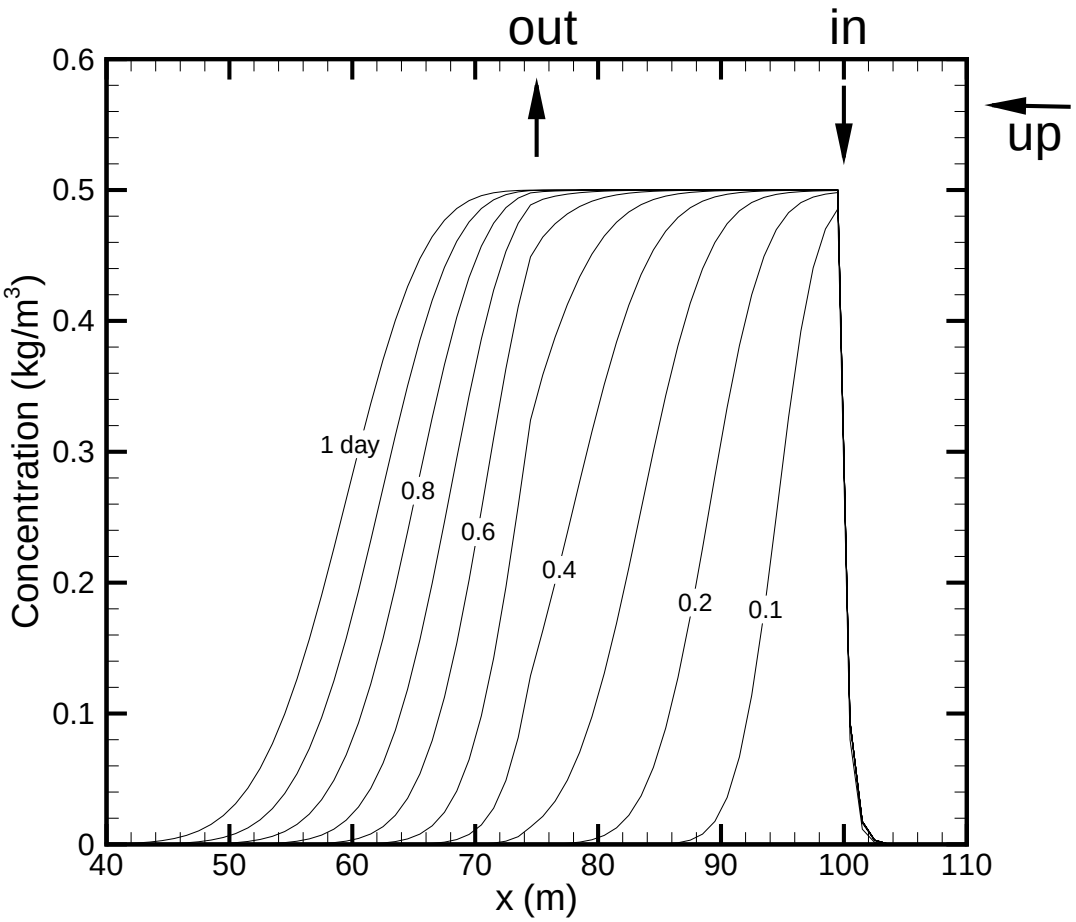

Figure 2.6. Simulated concentration profiles obtained at long times for widely separated inflow and outflow points.

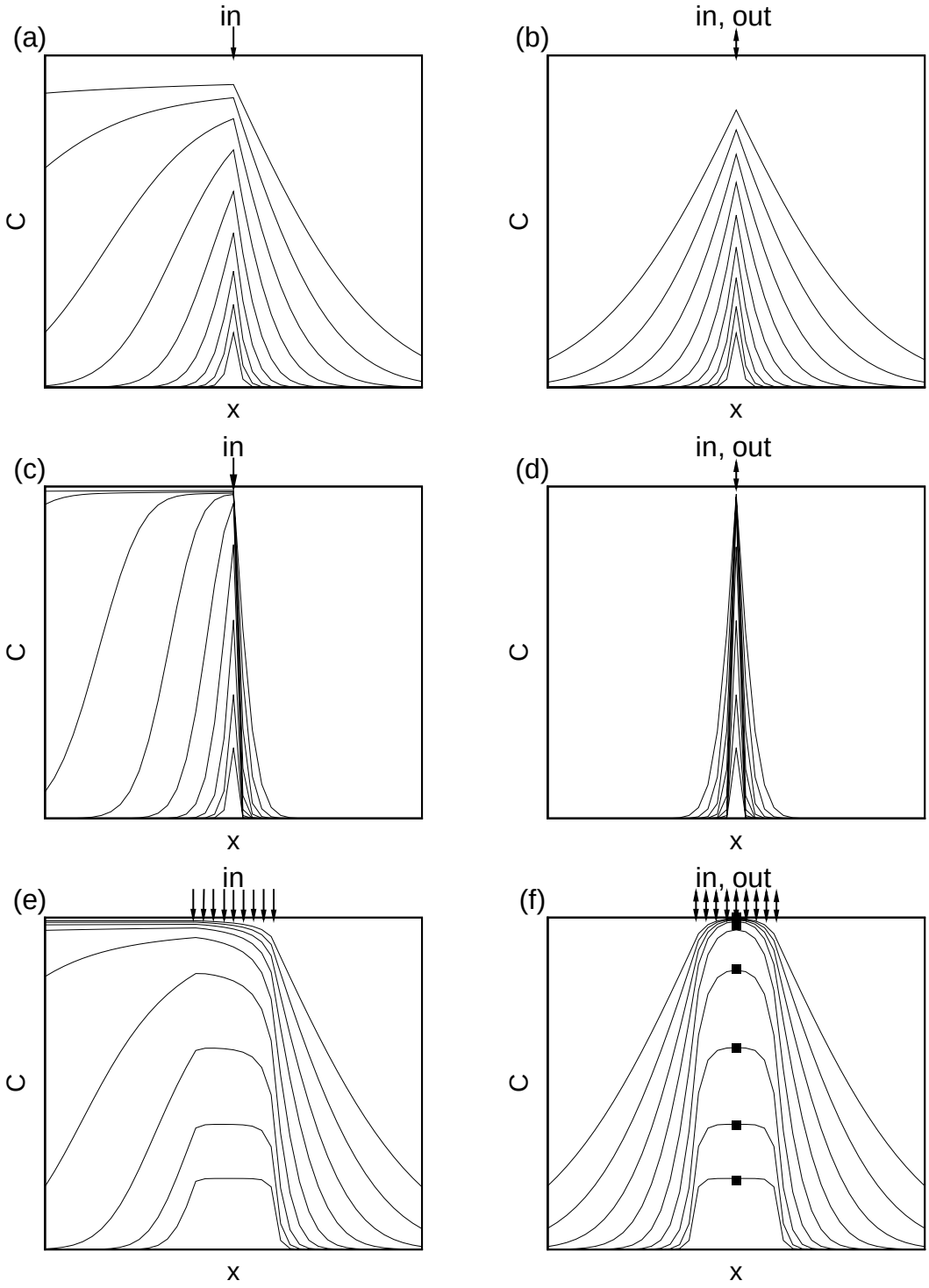

Figure 2.7. Simulated concentration profiles comparing inflow and horizontal flow for (a) a single inflow point; (b) a thin layer of horizontal flow; (c) a single inflow point with little longitudinal diffusion; (d) a thin layer of horizontal flow with little longitudinal diffusion; (e) a thick inflow zone; and (f) a thick layer of horizontal flow and the Drost et al. (1968) analytical solution (symbols). The time interval doubles between successive concentration profiles.

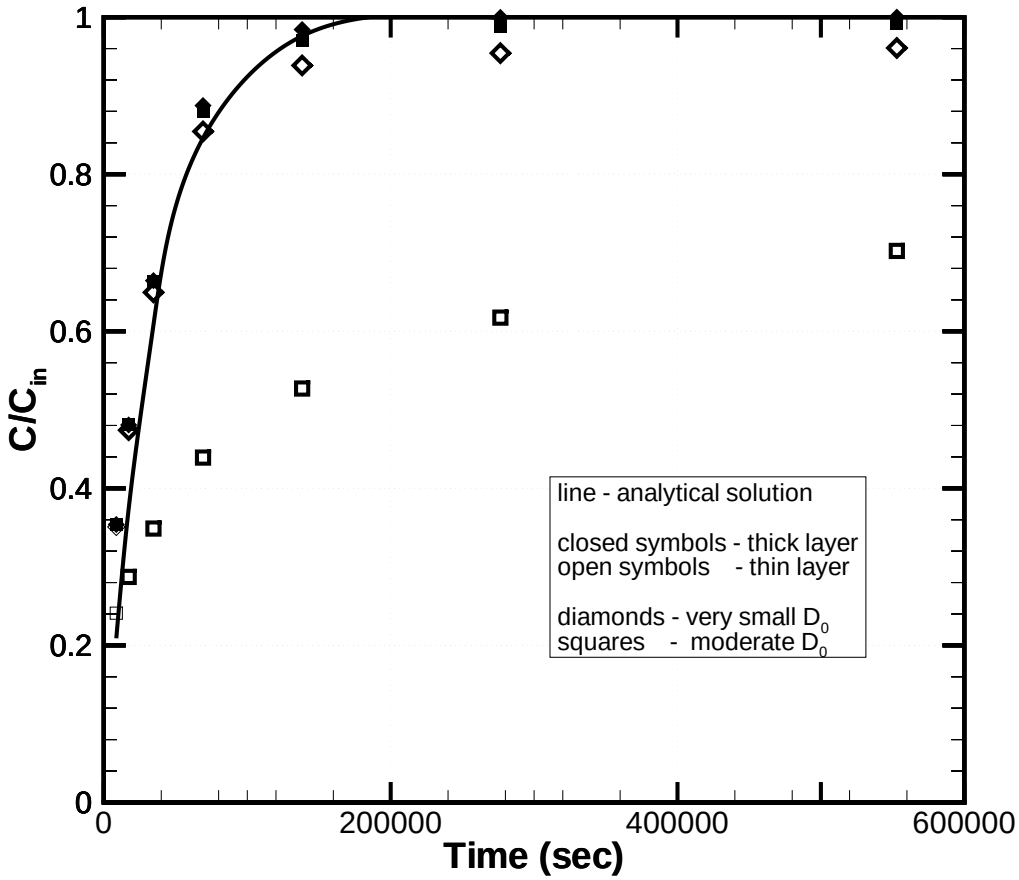

Figure 2.8. Simulated concentration versus time curves for the horizontal flow cases shown in Figure 2.7b, d, and f, as well as for a thick layer with little longitudinal diffusion and the Drost et al. (1968) analytical solution.

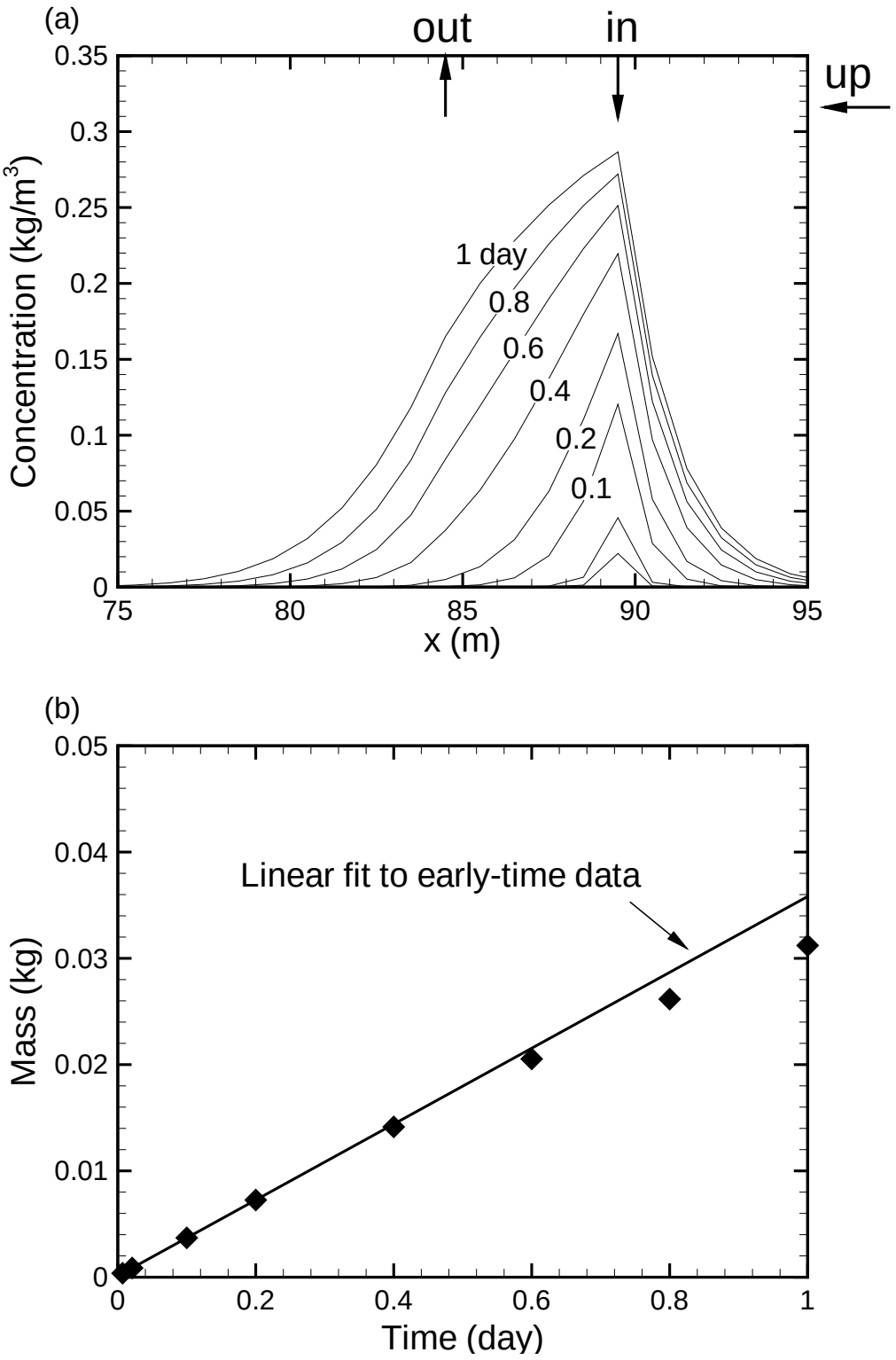

Figure 2.9. Short-time example of the mass integral method: (a) simulated concentration profiles; and (b) $M(t)$ integral and linear fit to early points.

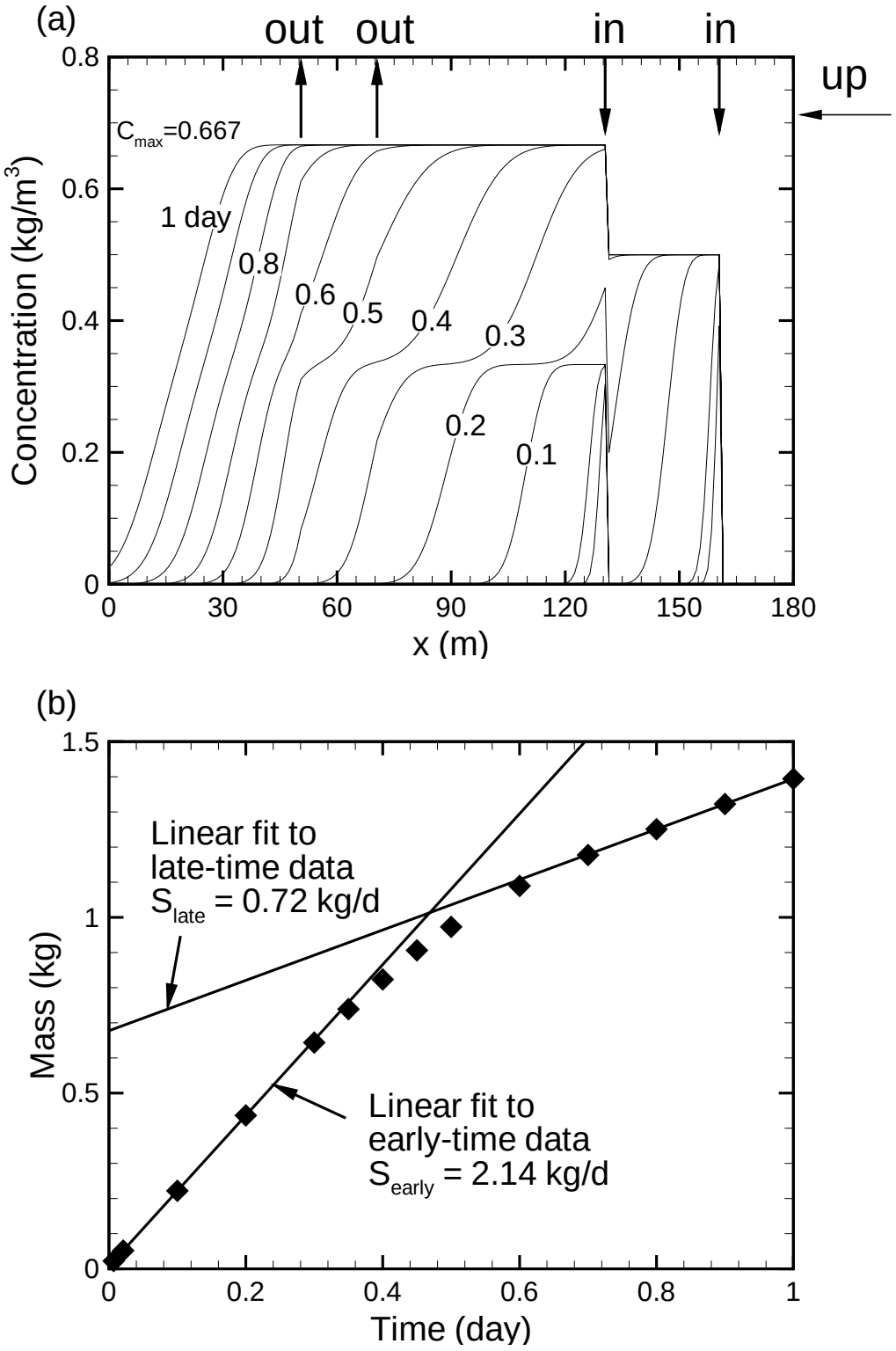

Figure 2.10. Long-time example of the mass integral method: (a) simulated concentration profiles; and (b) $M(t)$ integral and linear fits to early and late points.

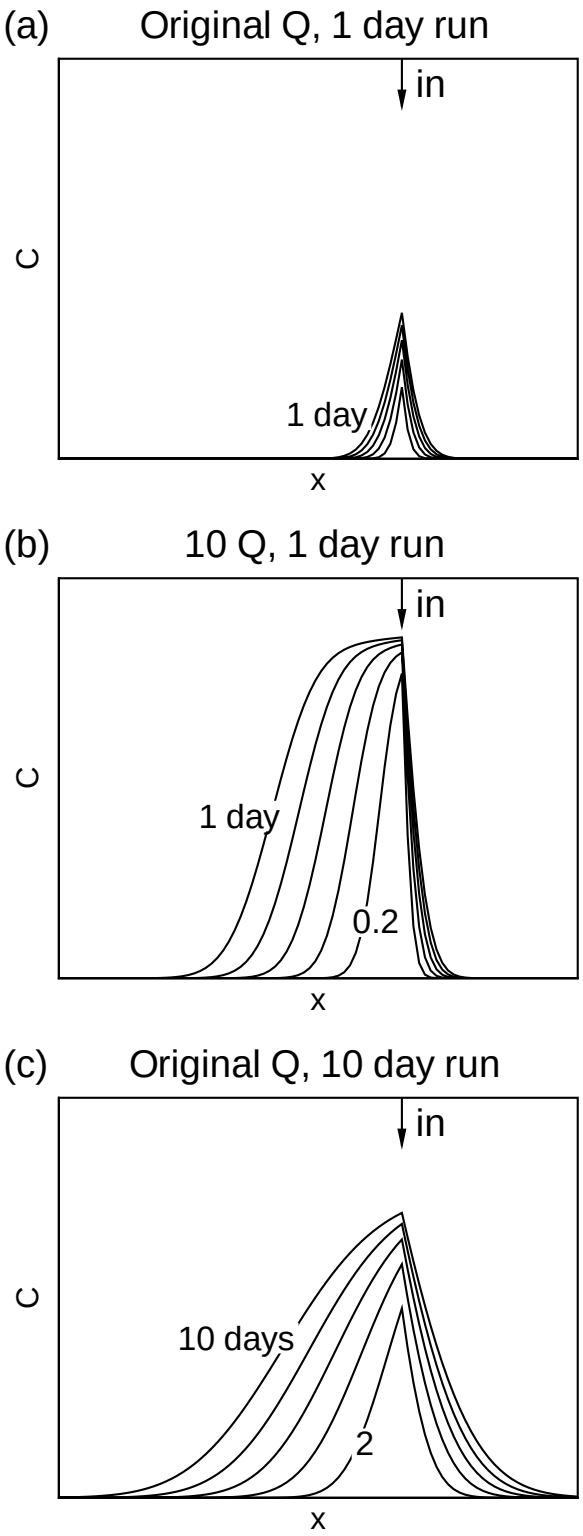

Figure 3.1. The effect of varying Q on concentration profiles for a single inflow point. On each plot, the profiles are equally spaced in time.

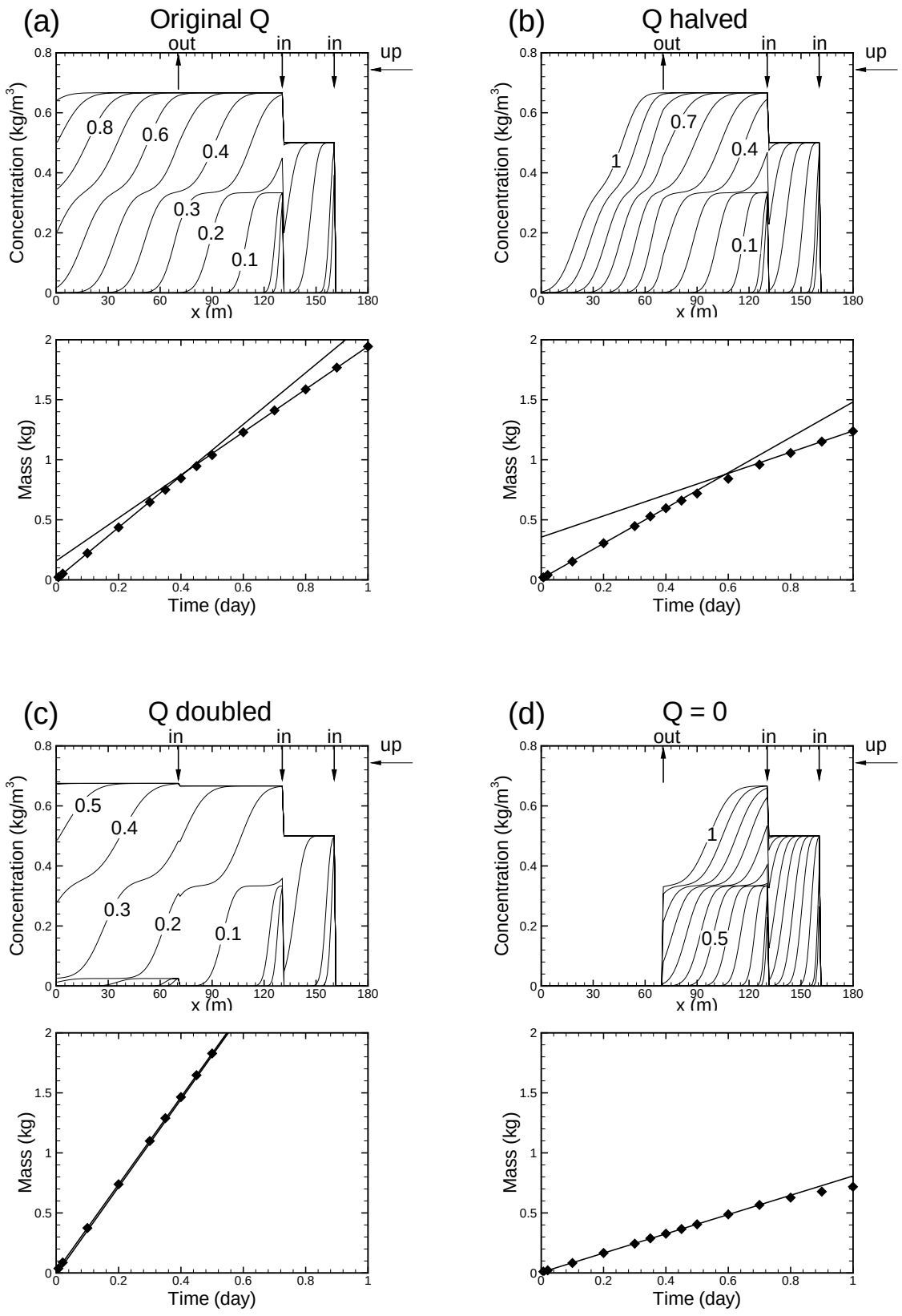

Figure 3.2. The effect of varying Q on concentration profiles and mass integral for inflow and outflow points when all T_i's are the same.

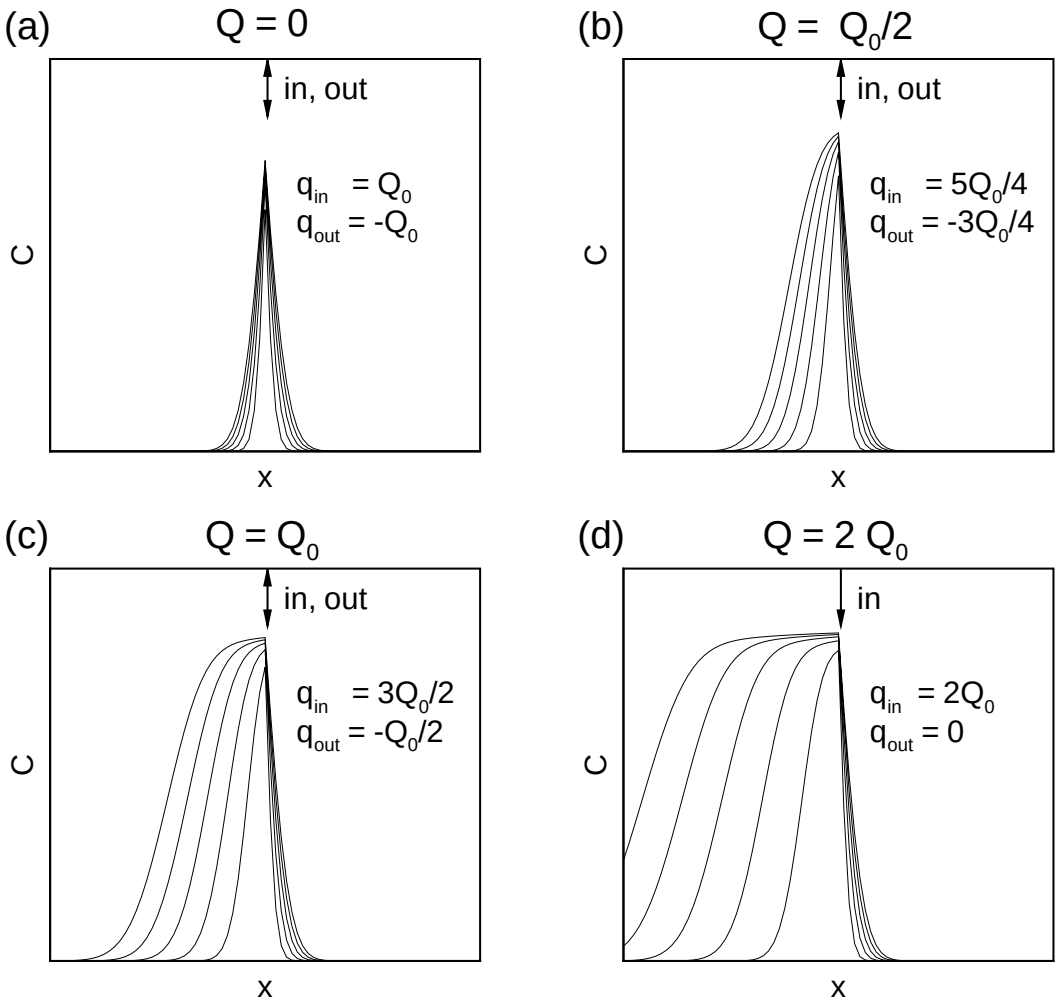

Figure 3.3. The effect of varying Q on concentration profiles for horizontal flow Q_0: (a) $Q = 0$; (b) $Q = Q_0/2$; (c) $Q = Q_0$; and (d) $Q = 2Q_0$. The profiles are equally spaced in time.

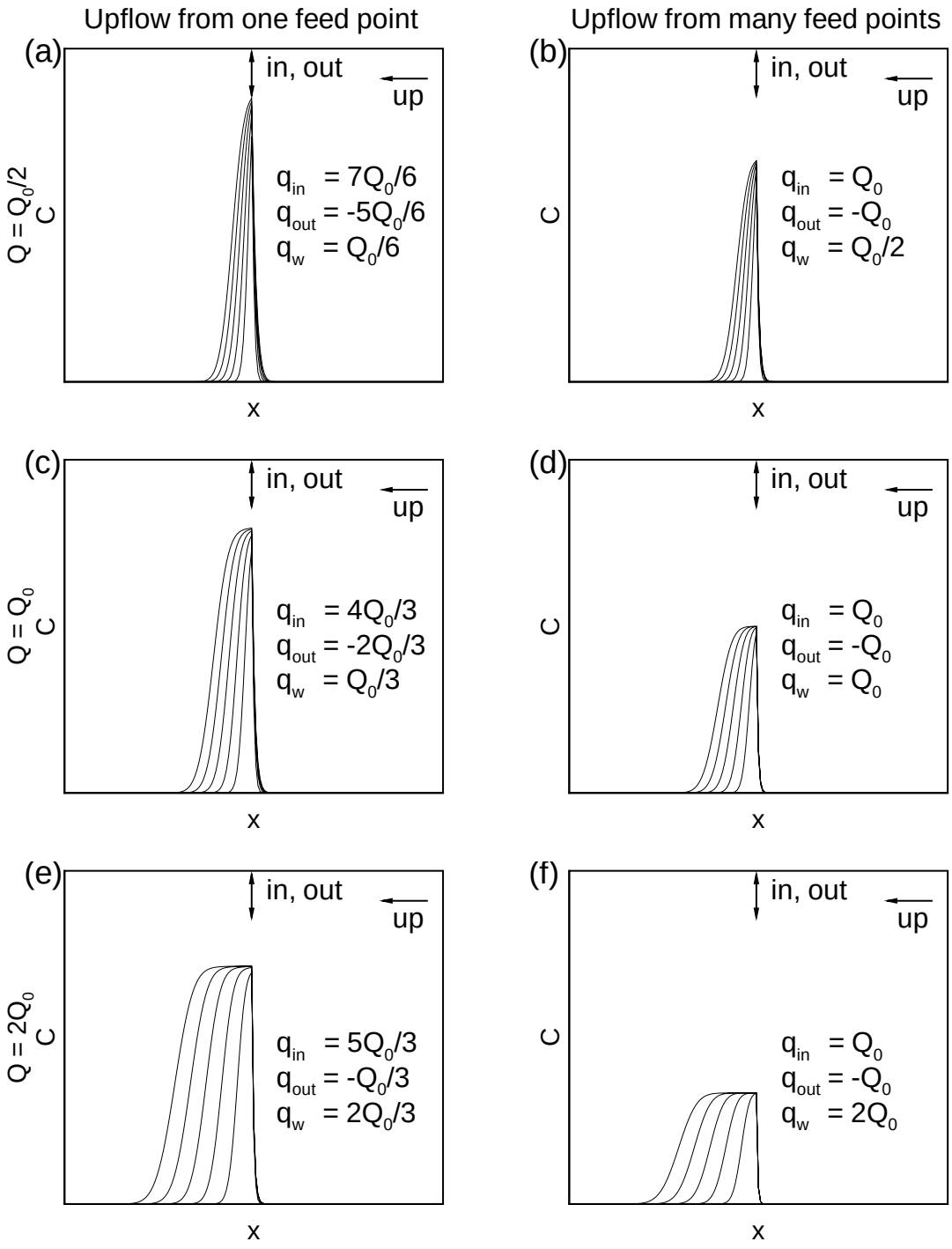

Figure 3.4. The effect of varying Q on concentration profiles for horizontal flow Q_0 when upflow is present: (a) and (b) $Q = Q_0/2$; (c) and (d) $Q = Q_0$; (e) and (f) $Q = 2Q_0$. In the left column, upflow is from one inflow point; in the right column, upflow is from an extensive recharge zone. The profiles are equally spaced in time.

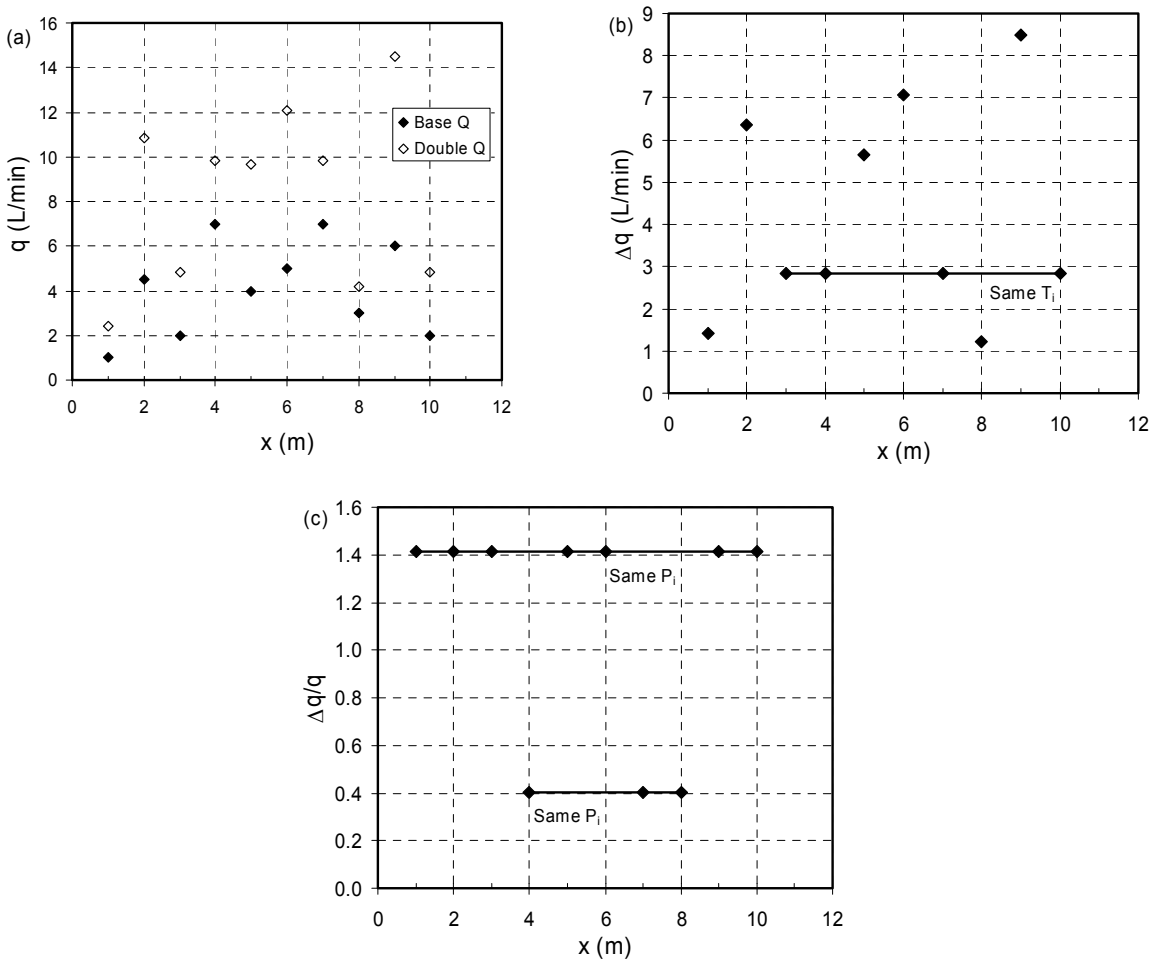

Figure 3.5. The effect of varying Q on inflow rates q_i: (a) inflow rates for base Q and doubled Q; (b) Δq for each feed point (feed points with the same Δq_i have the same T_i); (c) $\Delta q/q$ for each feed point (feed points with the same $\Delta q/q$ have the same P_i).

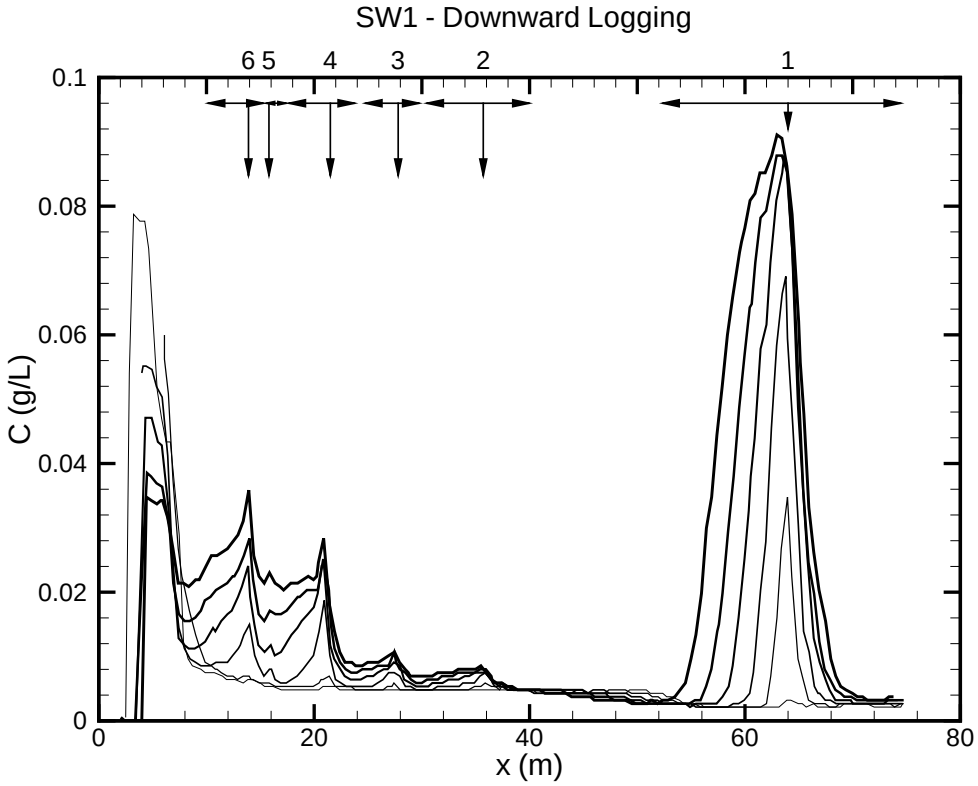

Figure 4.1. Concentration profiles obtained from borehole electrical conductivity logging of well SW1 at the Raymond field site in California (K. Karasaki, personal communication, 2001; see also Karasaki et al., 2000). Equation (A.1) is used to convert FEC to *C*. Concentration profile times (in minutes) are 1.8, 14, 25, 39, 52, and 66, with later profiles shown as thicker lines. The vertical arrows identify feed point locations and the horizontal arrows indicate the integration range for the corresponding peak.

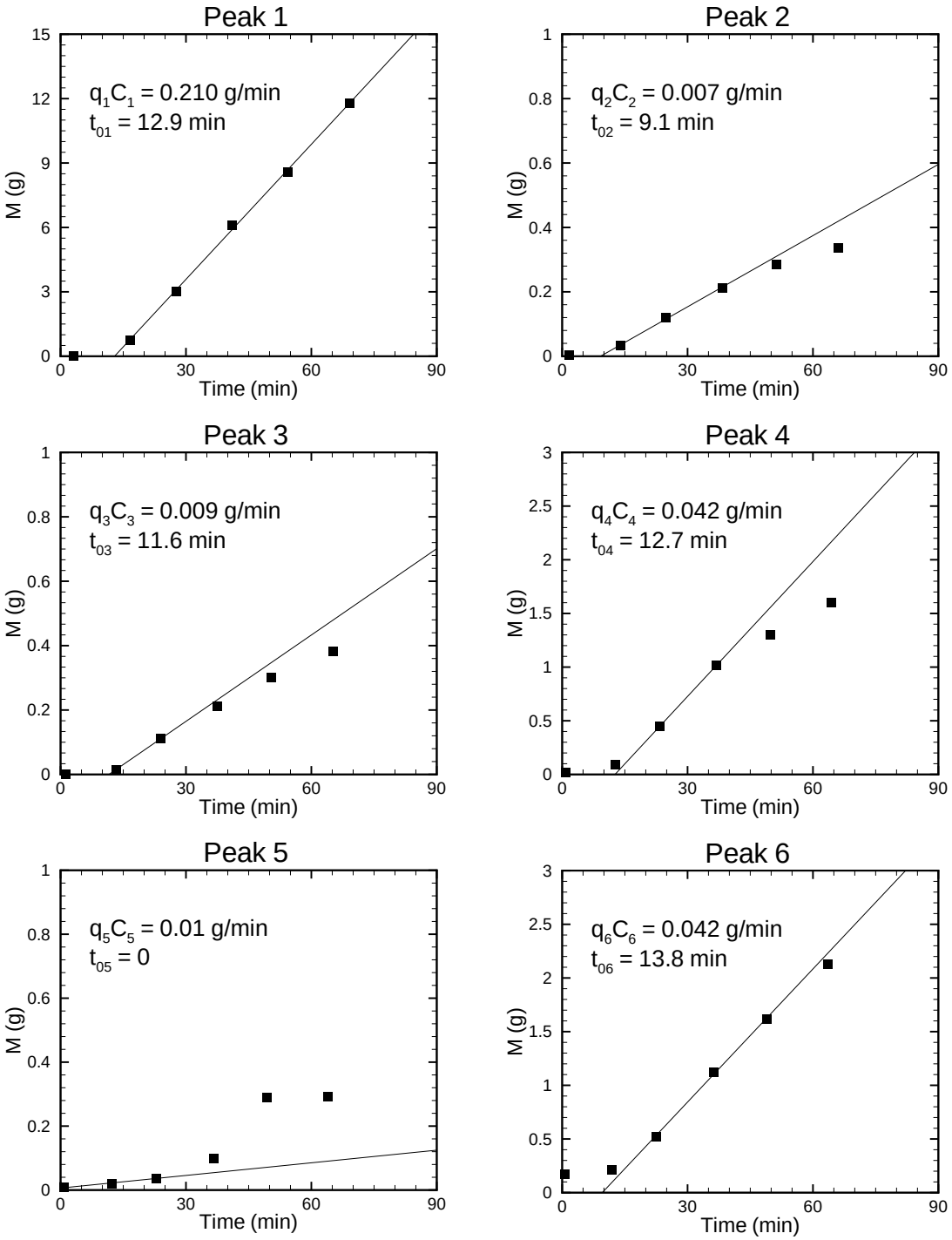

Figure 4.2. Mass integrals $M_i(t)$ for the six concentration peaks shown in Figure 4.1 and the linear fits used to determine q_iC_i (slope) and t_{0i} (time-axis intercept).

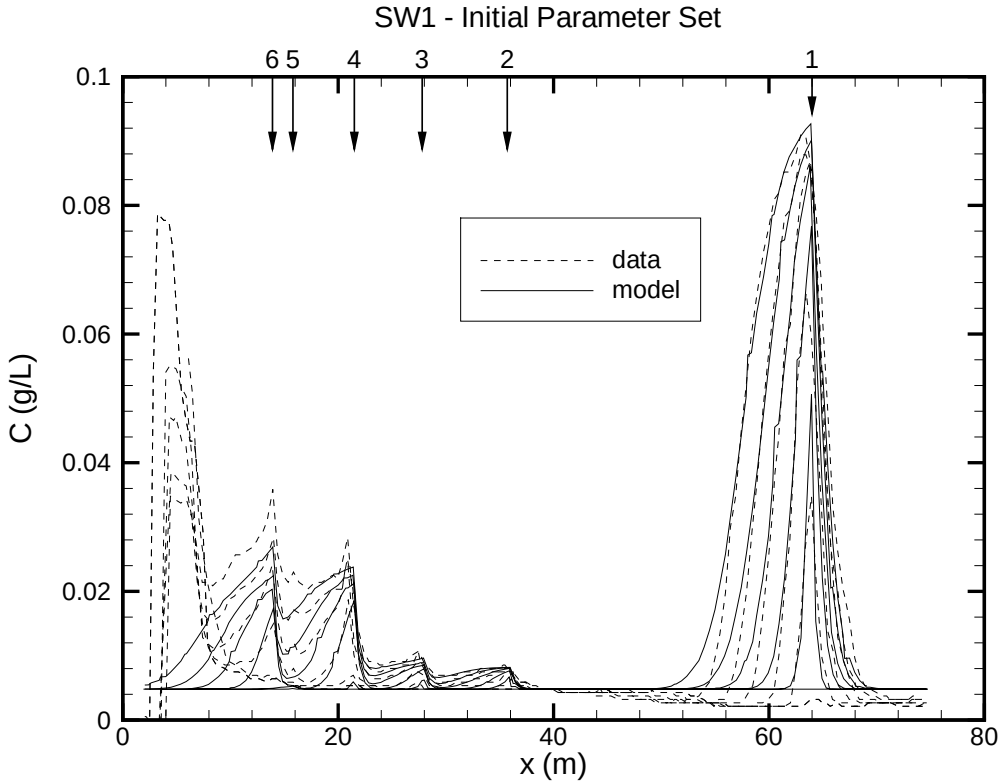

Figure 4.3. Comparison of observed and simulated concentration profiles for Raymond well SW1 for the initial parameter set (Table 4.1), obtained by analysis of observed concentration profile signatures.

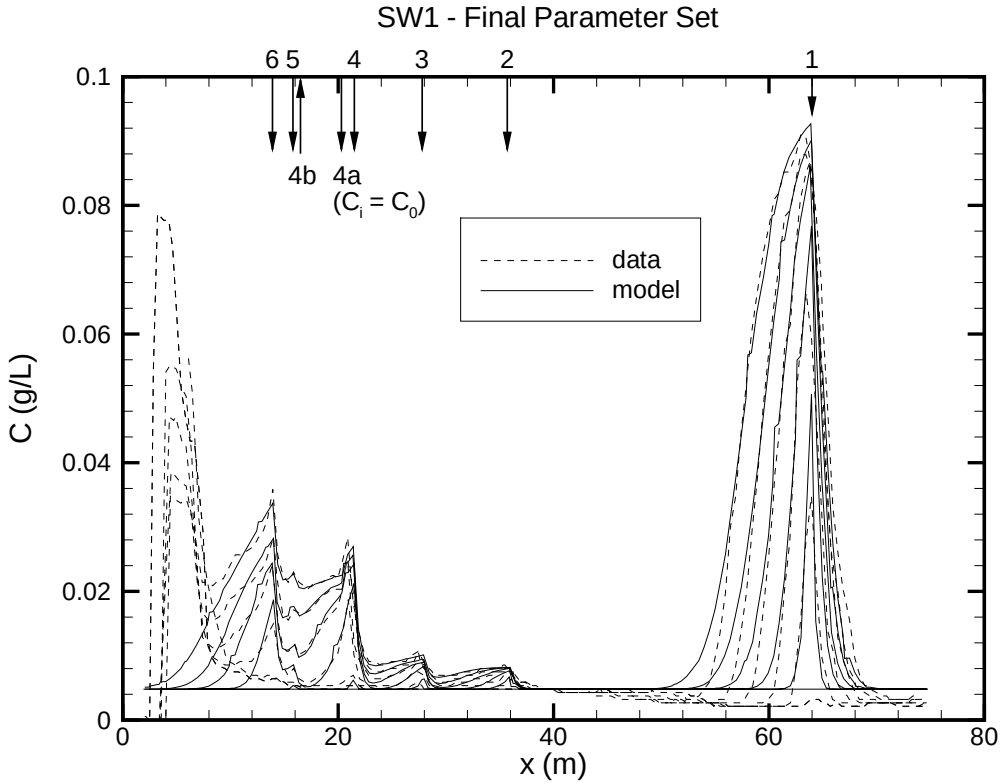

Figure 4.4. Comparison of observed and simulated concentration profiles for Raymond well SW1 for the final parameter set (Table 4.2), obtained by trial and error fitting with BORE II.

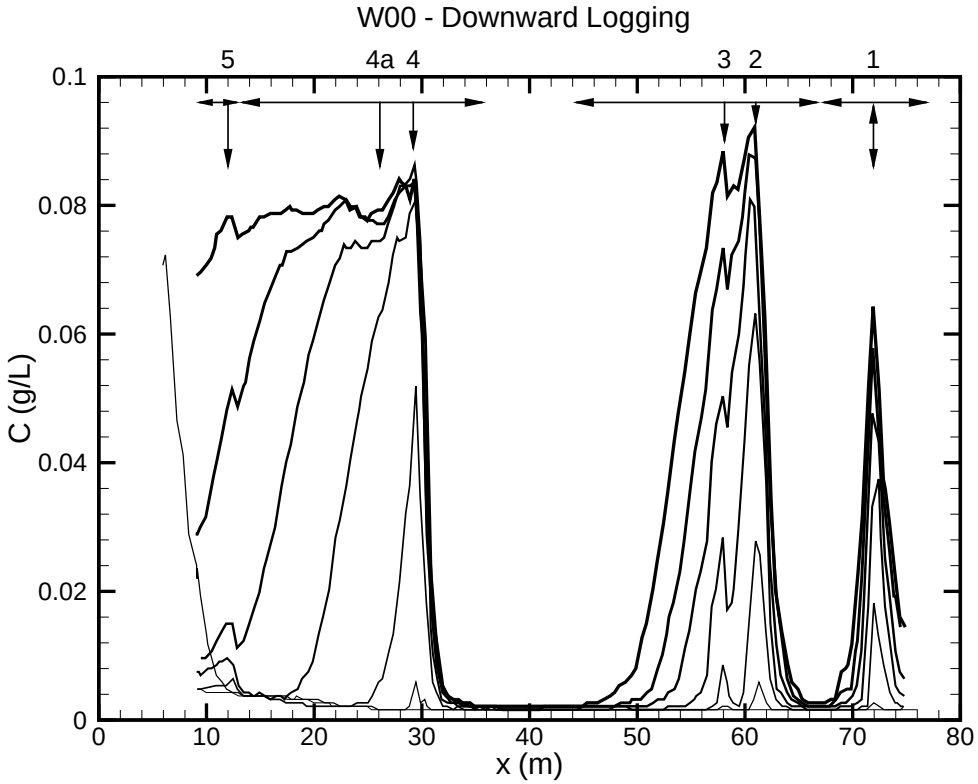

Figure 4.5. Concentration profiles obtained from borehole electrical-conductivity logging of well W00 at the Raymond field site in California (K. Karasaki, personal communication, 2000). Equation (A.1) is used to convert FEC to *C*. Concentration profile times (in minutes) are 3.5, 15, 26, 38, 51, 62, and 99, with later profiles shown as thicker lines. The vertical arrows identify feed-point locations and the horizontal arrows indicate the integration range for the corresponding peak.

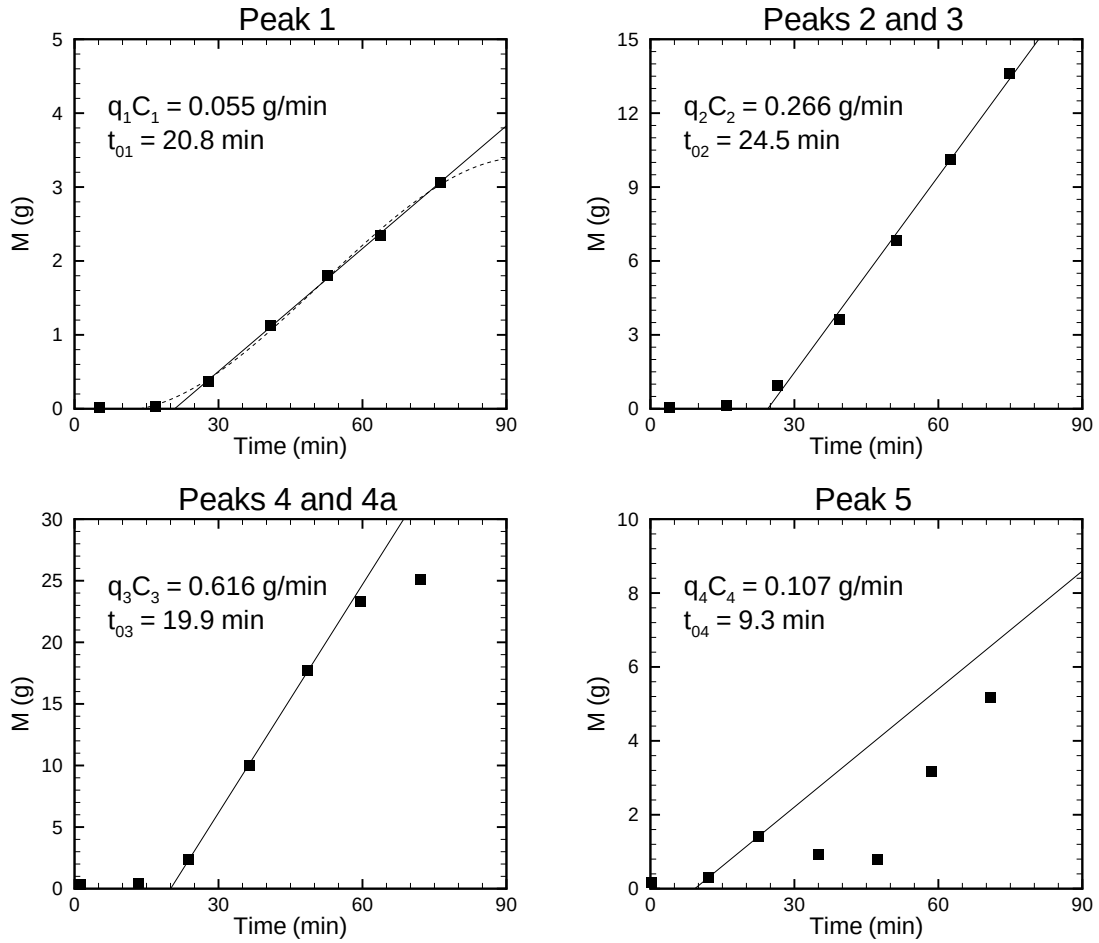

Figure 4.6. Mass integrals $M_i(t)$ for four of the concentration peaks shown in Figure 4.5 and the linear fits used to determine q_iC_i (slope) and t_{0i} (time-axis intercept). For Peak 1, the cubic curve fit to $M_1(t)$ (dashed line) may be used to determine a time-dependent C_1.

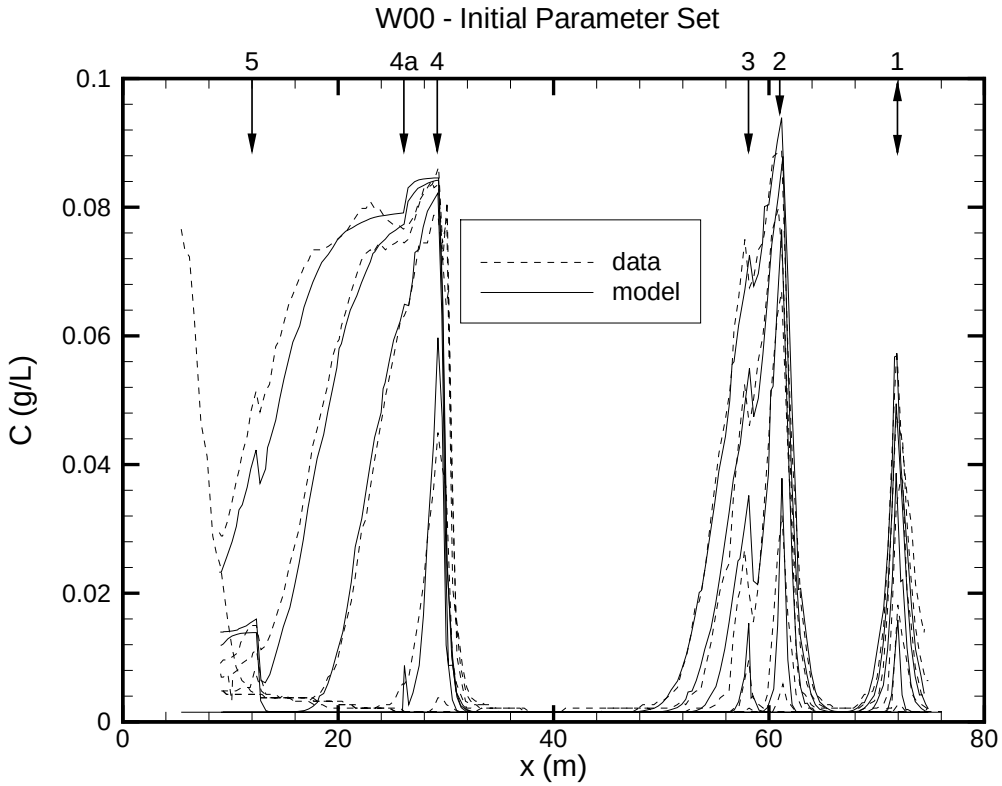

Figure 4.7. Comparison of observed and simulated concentration profiles for Raymond well W00 for the parameter set (Table 4.3) obtained by analysis of observed concentration profile signatures.

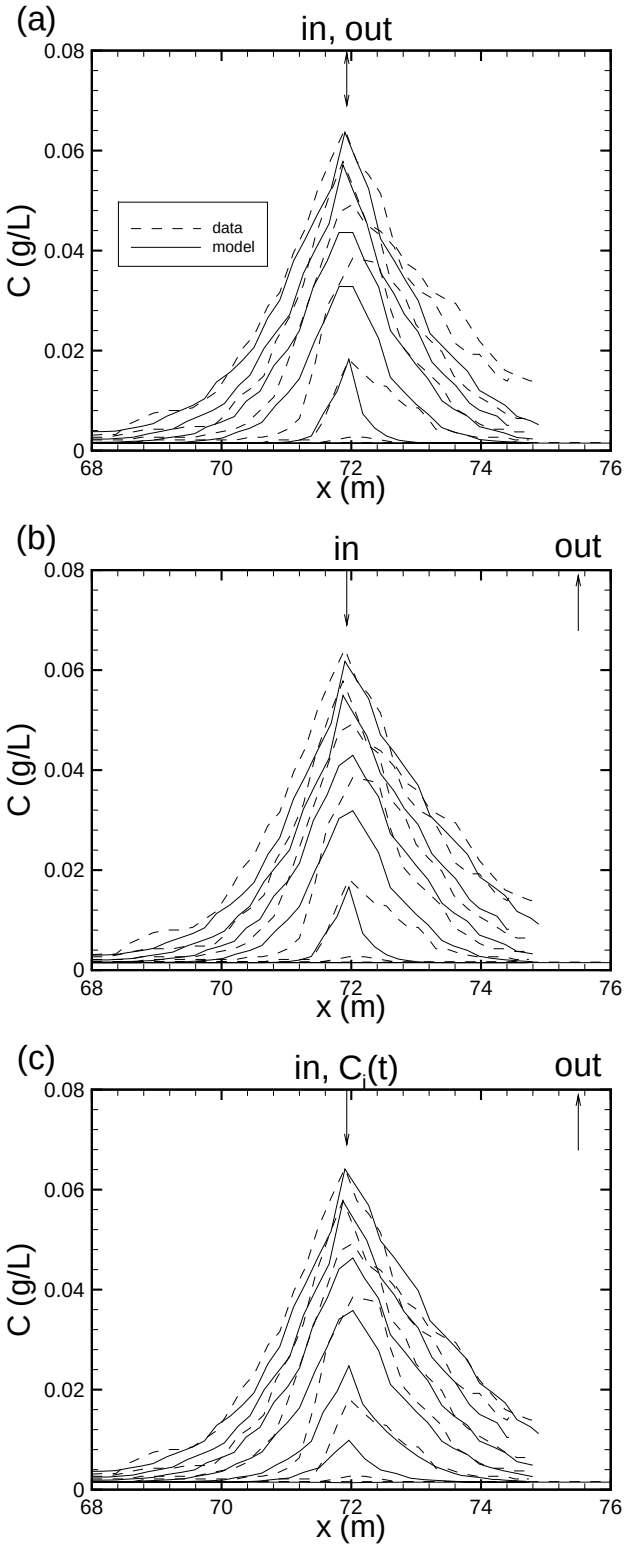

Figure 4.8. Comparison of observed and simulated concentration profiles for the lowest peak of Raymond well W00: (a) horizontal flow; (b) inflow with constant C_1 above outflow; and (c) inflow with variable $C_1(t)$ (see Figure 4.6) above outflow.

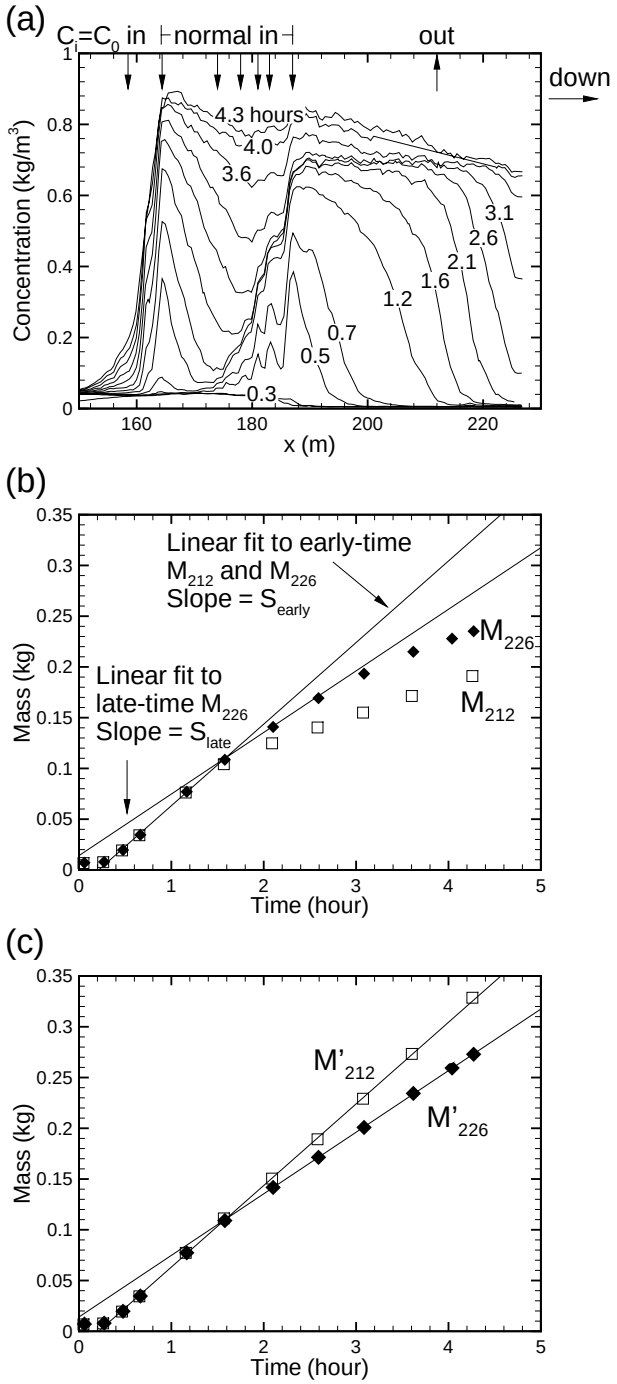

Figure 4.9. Use of the mass-integral method to identify an outflow point: (a) $C(x)$ profiles; (b) $M(t)$ integral for the entire wellbore section (M_{226}) along with linear fits to early and late points, and $M(t)$ integral for the wellbore section above the outflow point (M_{212}); and (c) corrected $M(t)$ integrals for the entire wellbore section (M_{226}') and for the section above the outflow point (M_{212}'). The lines show the linear fits used for the left-hand-sides of Equations (4.3) and (4.4) and the symbols show the right-hand-sides incorporating the optimal values of q_{226} and q_{212}.

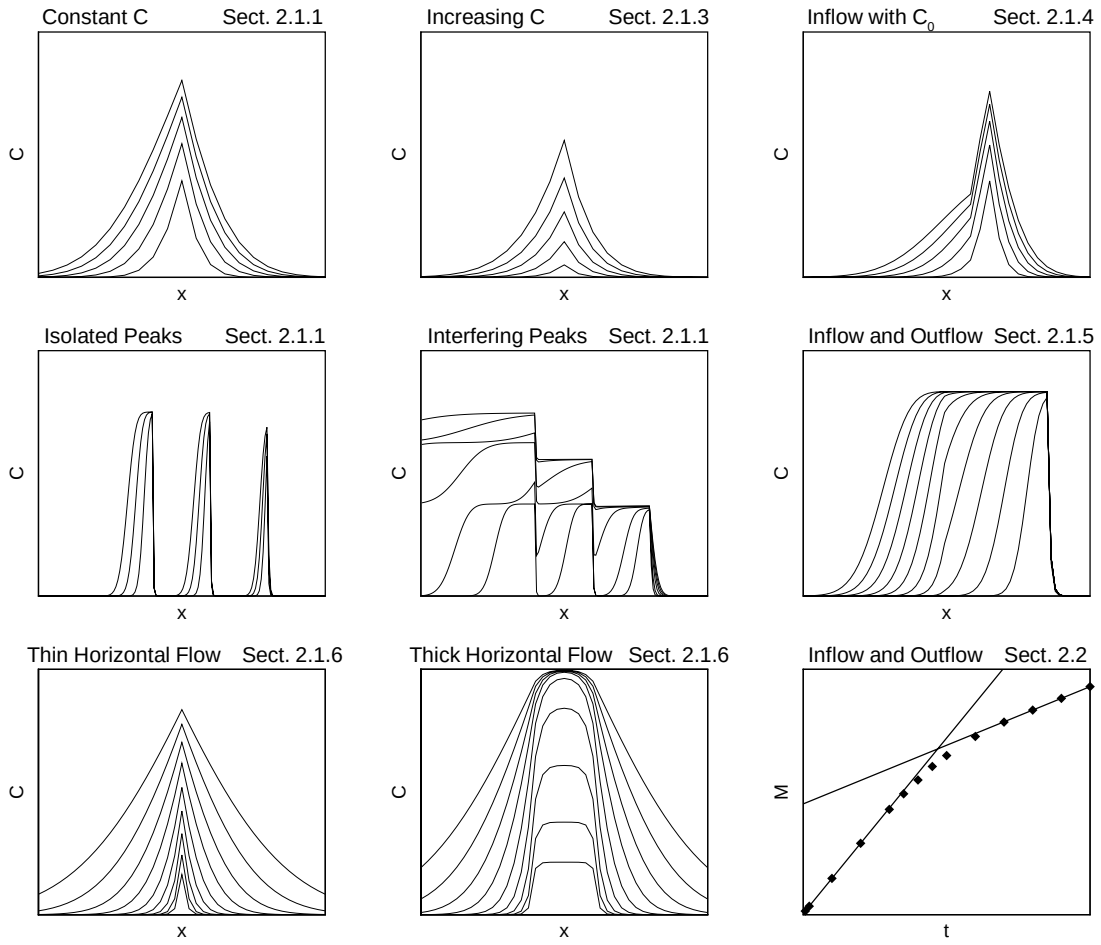

Figure 5.1. Overview of the $C(x)$ and $M(t)$ signatures discussed in this paper, along with the section number where each is presented.